

# *Kepler*’s dark worlds: A low albedo for an ensemble of Neptunian and Terran exoplanets

Tiffany Jansen<sup>1\*</sup> and David Kipping<sup>1</sup>

<sup>1</sup>*Dept. of Astronomy, Columbia University, 550 W 120th Street, New York NY 10027*

Accepted . Received ; in original form

## ABSTRACT

Photometric phase curves provide an important window onto exoplanetary atmospheres and potentially even their surfaces. With similar amplitudes to occultations but far longer baselines, they have a higher sensitivity to planetary photons at the expense of a more challenging data reduction in terms of long-term stability. In this work, we introduce a novel non-parametric algorithm dubbed *phasma* to produce clean, robust exoplanet phase curves and apply it to 115 Neptunian and 50 Terran exoplanets observed by *Kepler*. We stack the signals to further improve signal-to-noise, and measure an average Neptunian albedo of  $A_g < 0.23$  to 95% confidence, indicating a lack of bright clouds consistent with theoretical models. Our Terran sample provides the first constraint on the ensemble albedo of exoplanets which are most likely solid, constraining  $A_g < 0.42$  to 95% confidence. In agreement with our constraint on the greenhouse effect, our work implies that *Kepler*’s solid planets are unlikely to resemble cloudy Venusian analogs, but rather dark Mercurian rocks.

**Key words:** eclipses — planets and satellites: detection — methods: numerical — stars: planetary systems

## 1 INTRODUCTION

The amount of light reflected and emitted from an exoplanet is a direct probe of said planet’s surface or atmospheric composition. Several observational strategies have been successful in detecting this light, including high-dispersion Doppler spectroscopy (Snellen et al. 2010; Birkby et al. 2013), occultation detections both photometrically (Deming et al. 2005) and spectroscopically (Charbonneau et al. 2008), and photometric phase curves (Knutson et al. 2007). The study of these planetary photons, particularly when coupled with transit spectroscopy (Seager & Sasselov 2000; Charbonneau et al. 2002), has been instrumental in shaping our understanding of exoplanetary atmospheres to date (Burrows 2014).

In cases where these planetary photons are detected and the planet is known to be a transiting body, it is usually possible to measure the planetary albedo. This is achieved by noting that the occultation and phase curve amplitude is approximately equal to the geometric albedo multiplied by  $(R_p/a)^2$  (Winn 2010), and the planetary radius and semi-major axis in units of the stellar radius ( $p$  and  $a_R$ ) can be measured using the transit itself (Seager & Mallén-Ornelas 2003). Contextually, measuring an albedo close to unity implies that the planet is more likely to have an abundance

of highly reflective cloud coverage or have an icy surface, rather than, say, a bare surface darkened by basaltic rock (Hu et al. 2012). The shape of a planet’s phase curve can also provide insight into a planet’s thermal properties; for example an offset of the peak from the point of occultation implies a certain degree of heat redistribution from the sub-stellar point (Knutson et al. 2007) or asymmetric reflection from patchy clouds (Demory et al. 2013). In any case, measuring the amplitude and shape of phase curves allows us to identify individual planetary characteristics, which furthers our understanding of planetary compositions on a broader scale.

Amongst the various means of detecting planetary photons, photometric occultations and phase curves are particularly attractive from a data perspective, since transit survey missions, such as *Kepler*, collect long baselines of thousands of planetary systems at high precision. Further, although both the phase curve and occultation effects have similar amplitudes, the signal to noise ratio (SNR) is actually far superior using the phase curve method. This is because the phase curve temporal baseline is increased by the ratio of the orbital period to the occultation duration, which in turn should improve the SNR as  $\sim t^{1/2}$ . As an example of this, the amplitude of TrES-2b was first detected using just five months of *Kepler* data from the phase curve (Kipping & Spiegel 2011), giving  $(6.5 \pm 1.9)$  parts per million (ppm), be-

\* E-mail: jansent@astro.columbia.edu

fore being later found in occultation by collating 2.7 years of *Kepler* data (Barclay et al. 2012), giving  $(6.5 \pm 1.8)$  ppm.

As eluded to, *Kepler* data has already been used to detect numerous individual optical phase curves (Borucki et al. 2009; Kipping & Spiegel 2011; Esteves et al. 2013; Angerhausen et al. 2015), although primarily for Jupiter-sized planets on short-periods, such as HAT-P-7b. This is largely as a result of the strong detection bias intrinsic to the method itself, with the amplitude of the effect scaling as  $(R_p/a)^2$  (Winn 2010). For example, a  $1.5 R_\oplus$  Super-Earth with a geometric albedo of  $A_g = 0.5$  orbiting a Sun-like star at 0.05 AU would have a reflection amplitude below 1 ppm, making it exceedingly challenging for *Kepler* which has a median sensitivity of  $\sim 40$  parts per million (ppm) for a 12<sup>th</sup> magnitude star (Christiansen et al. 2013). Consequently, meaningful constraints on individual albedos are simply unobtainable for almost all Terrian and many Neptunian exoplanets found by *Kepler*.

As noted earlier, a major increase in the SNR is achievable by using phase curves rather than occultations, by essentially increasing the volume of data (Kipping & Spiegel 2011). Similarly, we propose in this work that a further increase in SNR can be achieved by stacking different planets (of similar type) together to create an ensemble phase curve. Although information about the individual planets is lost, this method enables a measurement of the average albedo for a collection of previously unobtainable small worlds.

This stacking approach has been used in numerous other examples recently, such as searching for exotrojans (Hippke & Angerhausen 2015) and exomoons (Teachey et al. 2018), but the most closely related example comes from Sheets & Deming (2014) who stack occultations. Stacking occultations is attractive since the effect is intrinsically localized and morphologically sharp, meaning simple local polynomial detrending can be used to correct for trends due to the instrument and stellar activity. However, as highlighted in the case of TrES-2b, occultations have considerably weaker SNR to planetary photons than the full phase curve (Kipping & Spiegel 2011). Nevertheless, Sheets & Deming (2014) appear to be first to appreciate the stacking opportunity and in that seminal paper measured an occultation depth of  $(3.8 \pm 1.1)$  ppm for an ensemble of 31 sub-Saturn ( $R < 6 R_\oplus$ ) *Kepler* planetary candidates. If the phase curve had zero contribution from thermal emission and was solely due to reflected light, the authors estimate this occultation depth corresponds to an average geometric albedo of  $A_g = (0.22 \pm 0.06)$ . In a follow-up study performed by the same authors, similar methods were applied to a larger ensemble, where they measured lower geometric albedos on the order of 0.1 (Sheets & Deming 2017).

In this study, we aim to maximize our sensitivity by stacking phase curves to measure the representative albedos of an ensemble of 50 Terrian planets and an ensemble of 115 Neptunian planets – the largest phase curve ensemble considered to-date. In Section 2, we describe our detrending and stacking methods, and define our target and ensemble criteria. In Section 3, we provide the expressions used to construct the phase curve models, and in Section 4 we describe our regression methods and model selection. In Section 5 we state our results for the two ensembles, which are then discussed in Section 6.

## 2 DATA PROCESSING

### 2.1 Frequently used detrending methods

In this work we seek to measure the phase curve signal of a large ensemble of *Kepler* exoplanets. Unlike when stacking the transits of many planets (e.g. Teachey et al. 2018) or the occultations (e.g. Sheets & Deming 2014), the signal of interest lasts for days and not just hours when considering full phase curves. Over timescales of days, significant variations are observed in *Kepler* time series, for example due to focus drift and intrinsic stellar activity, and these trends require removal before the phase curves of each planet can be co-added. The multi-day nature of the phase curve signal imposes the requirement of far greater long-term stability in the final data product than that typically needed when studying transits or occultations. As a result, many conventional detrending approaches are not well-suited for the task at hand.

For example, polynomial detrending would be inappropriate since even on the timescale of a few hours polynomial orders up to 4<sup>th</sup> order are often necessary (Sandford & Kipping 2017) for adequate detrending. Accordingly, for multi-day timescales, very high order polynomials would be needed, which become increasingly unstable. One solution to this is to use a moving polynomial kernel (e.g. Armstrong et al. 2016), although assuming a strict polynomial-shape for the variations does not have a clear motivation besides from mathematical convenience. Further, the order of the polynomial function must be selected, typically using metrics such as the Bayesian Information Criterion as a proxy for the full marginal likelihood. A problem with this is that often competing orders will score similar marginal likelihoods, meaning that formal Bayesian model averaging across an infinite sum of polynomial orders is necessary.

Another popular approach is cosine filtering, which was first developed specifically for phase curves analysis (Mazeh & Faigler 2010), although it has since found significant value in transit analysis too (e.g. Kipping et al. 2013). By adopting a Fourier-based approach, quasi-periodic signals should be expected to be more accurately described than polynomials which distort the power spectrum in unpredictable ways. However, since the cosine filtering comprises of a linear sum of cosine terms of ever higher orders, it too becomes unstable at high orders often necessary when studying trends over many days (Kipping et al. 2013). Similarly, the algorithm typically detrends using a linear sum of harmonic functions where the number of harmonics is fixed. As with polynomial detrending, this is somewhat unsatisfactory since increasing or decreasing the number of harmonics should lead to closely competing maximum likelihoods, meaning that formal Bayesian model averaging should be invoked.

To overcome these issues, non-parametric detrending methods are an attractive alternative. An obvious candidate would be median filtering, where one computes a moving median function at a specific kernel bandwidth over the entire time series and divides out the time series by this function. One popular choice for the bandwidth is of order  $\sim \mathcal{O}[10^1]$  consecutive points (e.g. Jenkins et al. 2015), but this would not be appropriate here. At such a small size, the method would remove not just the instrumental and stellar variations, but also the variations due to the phase curve itself. Rather than use a bandwidth based on consecutive points,

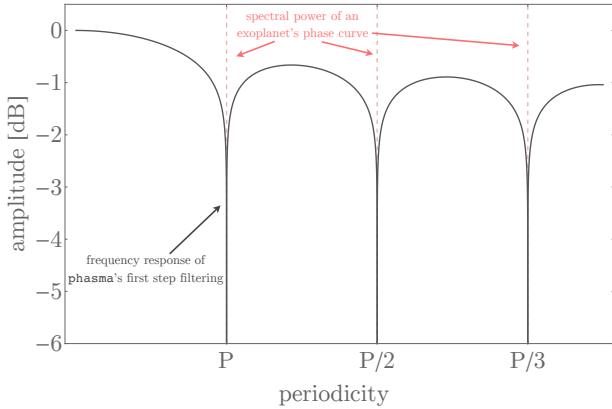


**Figure 1.** Spectral response function of applying a moving average filter with bandwidth  $P$  to a time series,  $F(t)$ , representing step 1 of **phasma**. The extreme attenuation at each harmonic removes any flux contributions from the planetary phase curve,  $F_P(t)$ , leaving behind a pure nuisance signal  $G(t)$ .

it is often preferable to use bandwidths with fixed temporal windows to account for potentially sparse data arrays. In this vein, a common choice is a longer bandwidth arbitrarily fixed to some value of order of days (e.g. [Rowe & Thompson 2015](#)), but such an approach is not designed or indeed intended to preserve phase curve functions.

## 2.2 Non-parametric detrending with phasma

To address the problems discussed above, we designed a new algorithm to detrend exoplanet phase curves that is simple yet powerful, which we refer to as **phasma**. Although similar non-parametric methods have been developed for extracting transit signals ([Samsing 2015](#)), **phasma** is instead optimized for phase curve recovery. The philosophy of **phasma** is that a planetary phase has a highly predictable spectral response function if the planet's orbital period is a-priori known, as is the case for transiting systems. Specifically, the phase curve will have strong power at  $\omega = 2\pi n/P$ , where  $n$  is the list of natural numbers to account for harmonics of the phase curve. This information could be used to design a filter that near-perfectly removes the planetary phase curve component of the original time series,  $F(t)$ , leaving behind a pure nuisance signal,  $G(t)$ . Finally, the nuisance signal can be then removed from the original time series to reconstruct the planetary phase curve, followed by phase folding and phase binning to enhance the final data product.

Although many band-stop filters could be considered to construct  $G(t)$ , an attractive option is the moving average. A moving average of bandwidth  $P$  has excellent attenuation at  $\omega = 2\pi/P$  and all higher harmonics (see Figure 1). Moreover, the filter is computationally cheap and conceptually simple. In practice, we elect to use a moving median filter instead of the mean, since it has the same spectral response properties but operates as a more robust estimator in the presence of outliers.

To illustrate **phasma**, consider taking the first data point of a photometric time series and then moving out to one orbital period later in time. If the data were solely due to a

phase curve, then this segment of data would encompass an entire phase curve and thus have a median equal to unity (for a normalized curve). If the data were due to a phase curve plus some nuisance signal, then similarly the phase curve contribution averages out and the median point is simply equal to the median level one would obtain if the signal were due to the nuisance signal alone. In this way, by moving along point-by-point with a kernel bandwidth of  $P$ , we trace out the nuisance signal exclusively.

**phasma** can be understood as comprising of the following three-step process

- (i) Construct a nuisance signal template using coherent median filtering
- (ii) Remove the nuisance signal from the original time series
- (iii) Phase-fold the residual signal to attenuate any non-coherent power

To formally prove the principle behind **phasma**, we provide here a mathematical description of the algorithm by defining the observed flux to be a linear sum of star's flux,  $F_*(t)$ , and the planet's flux  $F_P(t)$ . We explicitly assume that  $F_P(t)$  is a real-valued, strictly periodic function (although it need not be sinusoidal) and that the waveform of this function does not evolve in time (e.g. the amplitude does not vary in time), such that it exhibits translation symmetry:

$$F_P(t + nP) = F_P(t) \quad \forall n \in \mathbb{Z} \quad (1)$$

assuming the above means that the spectral response function of  $F_P$  exhibits line spectra located at  $\omega = 2\pi n/P$ , where  $n$  is a natural number, as depicted in Figure 1. In contrast,  $F_*(t)$  is not assumed to follow any particular functional form (although it is assumed to be real-valued), since indeed real stars can produce highly complex and intricate light curves. As mentioned earlier, in practice, the **phasma** algorithm uses a moving median, but we consider here using a moving mean for mathematical convenience, and explain the use of medians shortly. We further consider the time series to be well-approximated as being homoscedastic. **phasma** works by first constructing a nuisance signal time series,  $G(t)$ , which may be expressed as

$$\begin{aligned} G(t) &= \frac{\int_{t'=t-P/2}^{t'+P/2} [F_P(t) + F_*(t)] dt}{\int_{t'=t-P/2}^{t'+P/2} dt}, \\ &= \frac{\int_{t'=t-P/2}^{t'+P/2} F_P(t) dt}{\int_{t'=t-P/2}^{t'+P/2} dt} + \frac{\int_{t'=t-P/2}^{t'+P/2} F_*(t) dt}{\int_{t'=t-P/2}^{t'+P/2} dt} \end{aligned} \quad (2)$$

which may be re-written more compactly as

$$G(t) = \bar{F}_P + [F_* * \Pi](t). \quad (3)$$

In reality Equation 2 is performed as a sum of discrete observables, however we argue that the time sampling is much finer than the baseline and therefore any resulting discretization error is negligible. In Equation 3,  $\bar{F}_P$  is time-invariant, since marginalizing any periodic function over its period returns a constant, which is equal to the mean planetary flux in this case. In contrast, the second term preserves

time variability, where we have exploited the fact that a moving average is equal to the convolution of a gate function,  $\Pi(t)$ , with  $F_\star(t)$ , where

$$\Pi(t) = \begin{cases} 0 & \text{if } |t| > \frac{P}{2}, \\ 1 & \text{if } |t| \leq \frac{P}{2}. \end{cases} \quad (4)$$

It is instructive to consider the effect of the kernel on  $F_\star(t)$  in the frequency-domain, which can be derived taking the Fourier transform (which we denote as the operator  $\mathcal{F}$ ) of  $F_\star * \Pi$ . Via the convolution theorem,  $\mathcal{F}[F_\star * \Pi] = \mathcal{F}[F_\star] \cdot \mathcal{F}[\Pi]$ , and it is easy to show that

$$\mathcal{F}[\Pi(t)](\omega) = \frac{P \text{sinc}(P\omega/2)}{\sqrt{2\pi}}. \quad (5)$$

Since the sinc function's amplitude decreases as  $\omega^{-1}$ , high frequencies are attenuated, whereas low-frequencies pass through. Accordingly, let us write that

$$F_\star(t) = F_{\star,\text{low}}(t) + \Delta F_\star(t) \quad (6)$$

where the “low” subscript denotes the low frequency range (i.e. a periodicity which is greater than the period of the planet) and  $\Delta F_\star$  represents the residuals between the original function and its low-pass filtered component. Since  $F_\star(t)$  is a positive, real-valued function at all times (flux cannot be negative), then the moving average must also be positive and real-valued. By definition, the residuals of the original function around the moving average must therefore be real-valued but approximately equally mixed between positive and negative values. This point will become important when **phasma** performs a phase-folding operation later. Returning to Equation 3, we may now write that

$$G(t) = \bar{F}_P + F_{\star,\text{low}}(t). \quad (7)$$

Having constructed and defined  $G(t)$ , we now proceed to step 2 of **phasma** and remove  $G(t)$  from the original time series. The target function for the final phase curve function,  $\tilde{F}(t)$ , is defined in this work as being the planetary flux divided by the mean stellar flux,  $F_P/F_\star$ , in the case of perfect detrending. To achieve this, we can write

$$\tilde{F}(t) = \frac{F(t) - G(t)}{G(t)}, \quad (8)$$

which is equivalent to taking the original time series, dividing it by  $G(t)$ , and then subtracting unity (i.e. normalization + offsetting). Expanding out these functions using our earlier results, we have

$$\begin{aligned} \tilde{F}(t) &= \frac{[F_P(t) + F_\star(t)] - [\bar{F}_P + F_{\star,\text{low}}(t)]}{[\bar{F}_P + F_{\star,\text{low}}(t)]}, \\ &\simeq \left( \frac{F'_P(t)}{F_{\star,\text{low}}(t)} \right) + \left( \frac{\Delta F_\star(t)}{F_{\star,\text{low}}(t)} \right), \end{aligned} \quad (9)$$

where on the second line we have defined  $F'_P(t) = F_P(t) - \bar{F}_P$  (ultimately a constant offset does not affect our inference of the phase curve shape) and in the denominator used the  $F_{\star,\text{low}}(t) \gg \bar{F}_P$ .

The final step is to take  $\tilde{F}(t)$  and phase-fold upon the orbital period,  $P$ . Since  $F'_P(t)$  is periodic in  $P$ , and we fold exactly on  $P$ , then the signal is completely undisturbed by this process. In contrast, the  $\Delta F_\star(t)$  function is, in general, incoherent in  $P$  and is approximately evenly distributed between positive and negative values, by virtue of its construction (see earlier discussion). Accordingly, randomly sampling  $\Delta F_\star(t)$  and taking the mean will converge towards zero as we increase the number of samples, broadly following a  $N^{-1/2}$  scaling. In other words,  $\Delta F_\star(t)$  averages out on the phase fold.

We can get a quantitative handle on this attenuation by approximating  $\Delta F_\star(t)$  as a high frequency sinusoidal wave, for which the standard deviation of the signal is  $\simeq |\Delta F_\star|/\sqrt{2}$ , where  $|\Delta F_\star|$  is the sinusoidal amplitude. After conducting upon  $B/P$  folds (where  $B$  is the baseline of the time series), this is reduced to

$$\tilde{F}_{\text{fold}}(\phi) = \left( \frac{F'_P(\phi)}{\bar{F}_{\star,\text{low}}} \right) + \mathcal{O} \left[ \frac{\sqrt{P}}{\sqrt{2B}} \frac{|\Delta F_\star|}{\bar{F}_{\star,\text{low}}} \right], \quad (10)$$

where  $\phi$  is the orbital phase of the planet. Further attenuation of the residual stellar noise is then possible using phase-bins, since again the planetary signal remains coherent in the folded domain but the stellar component should not. Despite this, there remains a possibility for additional noise contamination by the star and thus we later show how cases with excess noise can be identified via the use of control system tests (see Section 2.6).

We highlight that in what has been represented thus far, the instrument response function has been ignored, but it is easy to see that it does not affect **phasma** so long as the instrument is dominated by low-frequency power. This can be seen from Equation 8, since an instrumental function acts as a product to  $F(t)$  and thus also  $G(t)$  and therefore is cancelled out in that equation, so long as the instrument function is largely unaffected by the convolution kernel. Quarter stitching is one way to introduce high frequency power, since step functions between each quarter would have high power in the frequency domain. For this reason, this work applies **phasma** on a quarter-by-quarter basis.

Because the kernel bandwidth is  $P$ , we cannot reconstruct the nuisance signal in the first and last  $P/2$  segments of the time series. Therefore we require that the baseline  $B \gg P$  so that the fraction of unreconstructed data is relatively small, and thus the method remains both robust and sensitive.

Finally, rather than using a moving average, **phasma** is run with a moving median as a more robust estimator for time series featuring outliers and flares.

### 2.3 Suitable phasma targets

A basic requirement for **phasma** is a precise measurement of each planet's orbital period. Since the planets considered in this work are transiting, then the period is indeed precisely known in all cases.

Each *Kepler* quarter is offset slightly from the surrounding quarters due to the rotation of the spacecraft causing the stars to appear on different CCDs of slightly different sensitivities. An attempt at correcting for this is made in the PDC-MAP data product (Smith et al. 2012; Stumpe et al.



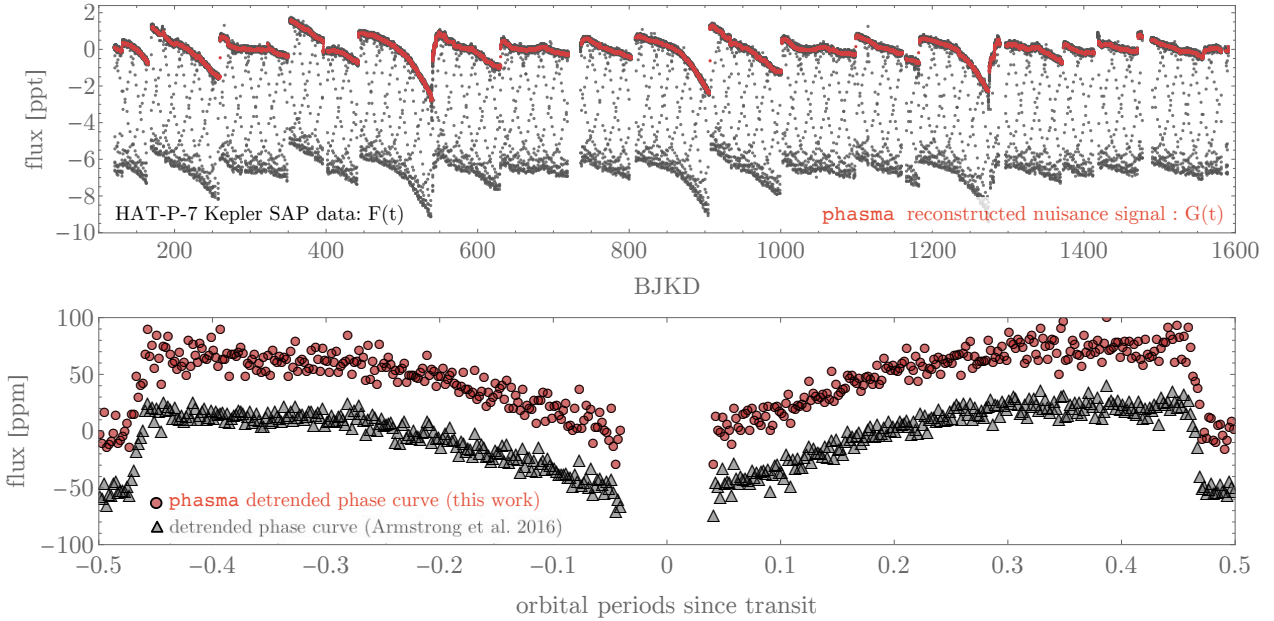


**Figure 2.** Top panel: SAP light curve of HAT-P-7, transits are clearly visible. We overlay the moving median function (red) adopting a kernel width of  $P$ . Lower panel: Resulting phase curve from our detrending (red circles, offset by +50 ppm) compared to the phase curve of [Armstrong et al. \(2016\)](#) (grey triangles) for the same system but derived using an independent method.

2012) although the associated uncertainty in that correction is unclear. For simplicity, we detrend each *Kepler* quarter independently, which means  $B \sim 90$  days. In order to satisfy  $B \gg P$  then, our targets are selected such that  $P < 10$  days.

In addition to this filter, we also eliminated systems with more than one planet, where the phase curves would co-add and negatively affect our detrending approach. Next, we only considered planets with a NASA Exoplanet Archive (NEA; [Akeson et al. 2013](#)) disposition of “CONFIRMED”.

Finally, we removed stars with logarithmic surface gravities less than 4. The  $\log(g)$  cut is motivated to remove stars with a higher false-positive rate ([Sliski & Kipping 2014](#)) as well as stars with increased activity signals, which have the potential to negatively influence our results. In doing so we attenuate the contamination from these objects and declare a well-defined cut to make our work reproducible.

Applying these cuts on September 29th 2016 gave us 477 Kepler Objects of Interest (KOIs) which we used in what follows.

#### 2.4 Applied example of phasma: HAT-P-7b

As an example of our detrending method, we showcase its performance for a well-known system, HAT-P-7b, which exhibits strong phase curve variations ([Borucki et al. 2009](#)). The simple aperture photometry (SAP) for this star is shown in Figure 2, where we have normalized each quarter by the median flux. Setting  $P = 2.204735417$  days as reported on NEA, we derive the median function, shown in red in the top panel of Figure 2, and then divide the original data through this function. End member data (within  $P/2$  of the quarter stitch points) are not reconstructed. In this example and the real analyses shown later, only the long-cadence data is used or necessary.

The data are then phase folded, centered upon the time of transit minimum, and the data binned to 500 evenly spaced phase points. Outliers exceeding  $5\sigma$  from each phase window are rejected. The final phase curve is shown in the bottom panel of Figure 2 which we compare to that presented in the independent analysis of [Armstrong et al. \(2016\)](#). Although [Armstrong et al. \(2016\)](#) used a moving polynomial based detrending, the two methods provide equivalent results and give us confidence that our algorithm performs as expected. Unlike [Armstrong et al. \(2016\)](#), there is no need with our method to experiment with different polynomial orders or kernel sizes, and the detrending options are fixed and objective enabling a fast and homogeneous detrending of hundreds of KOIs.

#### 2.5 Choosing a binning scheme

In order to homogenize the different phase curves of each KOI, we decided to bin the data into 500 evenly-spaced phase bins. We then removed all phase points occurring within 5% of the orbital period centered on the transit to ensure transits do not contaminate our sample, leaving 450 points.

For a given KOI, the point-to-point formal uncertainty estimates do not vary greatly throughout the time series and thus is approximately homoscedastic. We attempted four different binning schemes to create our binned phase curves for each individual KOI: a) simple mean b) weighted mean c) simple median d) weighted median. The weighted-options account for the modest degree of formal heteroscedasticity.

We binned all 477 KOIs in our sample with all four methods and then measured the median absolute deviation of the final binned light curve from each. We ranked the methods from best to worst for each KOI and then compiled

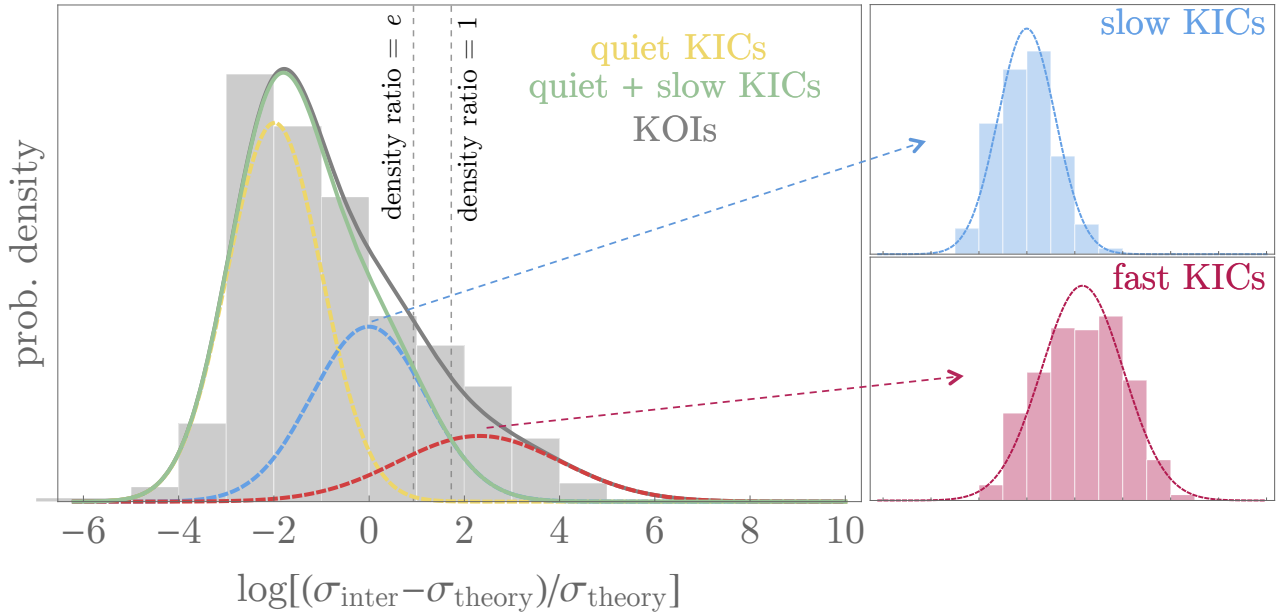


**Figure 3.** Right panels: Histograms showing the distribution of standard deviations obtained (normalized by a theoretical benchmark) for the slow rotating and fast rotating control sample. Left panel: Same as right except for the 477 KOIs considered in this work. The distribution is well described by a mixture model of the fast KICs, slow KICs and an additional quieter subsample. The density ratio of  $e$  between the quiet+slow and fast populations demarks our cut-off for acceptable noise properties.

the list of ranks for all KOIs. We find that the weighted mean is the method which ranks the highest, winning 477 of the 477 trials. Accordingly, we elected to adopt the weighted mean binning scheme in what follows.

## 2.6 Applying to control systems

After applying our detrending algorithm to all 477 KOIs, we required some way to assess whether the resulting phase curves were of acceptable quality. This required a point of comparison and thus we elected to run our code on two other samples of 477 targets, where no KOIs are presently known to reside to serve as control systems. The first group is dubbed as “slow KICs”, chosen since their rotation periods are slow and thus should be expected to display lower stellar activity than usual. The second group is dubbed the “fast KICs” for the opposite reason, since they have fast rotation and thus should have significant stellar activity.

The slow sample was defined such that rotation period was slower than 20 days, the effective temperature of the star was between 3000 K and 7000 K and the log surface gravity was greater than 4.0. The fast sample used the same cuts except the rotation period was required to be faster than 5 days. In both cases, we used the [Mcquillan et al. \(2014\)](#) rotation periods to perform these cuts and ensured no KOIs existed at the time of writing.

For the fast sample, we detrended the time series assuming a fictional orbital period randomly drawn from between 1 and 5 days. This represents a worst-case scenario for our method since these fictional orbital periods are nearly in phase with the intrinsic stellar variations. In the case of the slow sample, we draw a random orbital period from the same distribution, but here the intrinsic variations are expected

to be much slower than the kernel width, which should lead to a more precise detrending.

After detrending, we define the uncertainty on the phase curve points in two ways. First, we define  $\sigma_{\text{theory}}$  as being the uncertainty computed from a simple weighted mean calculation, thus equal to

$$\sigma_{\text{theory}} \equiv \sqrt{\sum_{i=1}^n \frac{1}{\sigma_i^2}}, \quad (11)$$

where  $\sigma_i$  are the SAP reported photometric errors and the sum is performed over a specific binning window. We find, as expected, for any given KOI that the 450 binned  $\sigma_{\text{theory}}$  are very similar and thus simply adopt their median value as a fixed point estimate for each unique KOI in what follows.

In addition to  $\sigma_{\text{theory}}$ , which represents a best-case scenario uncertainty, we also empirically measure the uncertainty in the final phase curve by computing the standard deviation. Since the phase curve of each KOI can exhibit significant variations due to the intrinsic phase curve signal, rather than noise, it is necessary to first perform a first-order removal of any such signal. To accomplish this, we use a simple linear least squares fit of composite sinusoidal model for the ellipsoidal variations, Doppler beaming and reflection+thermal component following Equation 6 of [Mazeh & Faigler \(2010\)](#). We then define  $\sigma_{\text{inter}}$  as the standard deviation of the residuals.

An idealized system would have  $\sigma_{\text{inter}} \simeq \sigma_{\text{theory}}$ , but persistent nuisance variations unaccounted for by our detrending are generally expected to inflate  $\sigma_{\text{inter}}$  above  $\sigma_{\text{theory}}$ . In this way, we identify the ratio ( $\sigma_{\text{inter}}/\sigma_{\text{theory}}$ ) as a key metric for assessing the quality of our detrending. Since in general we expected the best case to be unity, we subtract one from

this ratio and take the log to more clearly inspect the diversity of ratios found. Repeating for our three samples (the KOIs, slow KICs and fast KICs), we histogram the resulting ratio proxies in Figure 3.

As can be seen in Figure 3, the fast KIC sample exhibits a larger typical ratio than of the slow KICs, as should be expected, since our detrending algorithm is most likely to struggle in the fast regime.

Remarkably, the KOI sample displays an even lower ratio than that of the slow KIC control sample, implying that KOI host stars are less active than even the slow rotating *Kepler* stars. One possible explanation for this could be that a population of non-transiting planets are contaminating the slow KIC sample, thus generating a higher uncertainty ratio, however we find this explanation improbable. The number of transiting exoplanets that produce independently detectable phase curve amplitudes has been relatively low, and therefore we would expect to see a similar paucity of non-transiting planets with non-negligible phase curves in our slow KIC sample. Additionally, the phase curve amplitude is at its maximum when the orbit is along the line of sight and would therefore decrease for non-transiting exoplanets, further lowering the possibility of being responsible for the larger uncertainty ratio in the slow KIC sample. Instead, this is most likely an artifact of selection bias, since transit signals are intrinsically easier to detect around quieter stars.

We find that normal distributions well-describe both the slow and fast KIC histograms in Figure 3 and thus one can treat the KOI sample as being a mixture model of these two components plus some additional even quieter component. Assuming this additional component is also a normal distribution, we use maximum likelihood regression to find that the KOI sample is well-described by a mixture model of 16.2% fast KICs, 30.0% slow KICs and 53.7% an additional quiet sample component.

In general, we deem it satisfactory if a target star can be said to belong to either the quiet or slow KIC sample, since our detrending algorithm is designed with such cases in mind. Accordingly, using our mixture model, we remark that for all  $(\sigma_{\text{inter}}/\sigma_{\text{theory}}) < 6.6$ , it is more likely a sample would belong to the slow+quiet sample than the fast sample. At the critical ratio of 6.6, the probability density ratio between the two populations is unity, and thus for the sake of conservatism we push this back until the probability density ratio equals  $e$ , which occurs at  $(\sigma_{\text{inter}}/\sigma_{\text{theory}}) = 3.6$ .

In Figure 4 we show a scatter plot of the two noise estimates for the 477 KOIs and draw a line demarking the cut-off ratio of 3.6. This cut reduces our sample from 477 KOIs to 378, removing 99 targets.

## 2.7 Stacking different KOIs

Each binned phase curve has a slight but somewhat arbitrary offset that means simple stacking of the curves present noticeably poor coherence. It is therefore necessary to define an offset term for each KOI which is subtracted prior to the final stacking.

Consider the  $j^{\text{th}}$  binned phase point of the final stacked phase curve of all KOIs, where  $j = 1, 2, \dots, n_{\text{bins}} - 1, n_{\text{bins}}$  (where in our case  $n_{\text{bins}} = 450$ ). Within that bin, there are  $n_{\text{KOI}}$  data points, one from each KOI, contributing to the binned point. Ideally they would closely agree with each

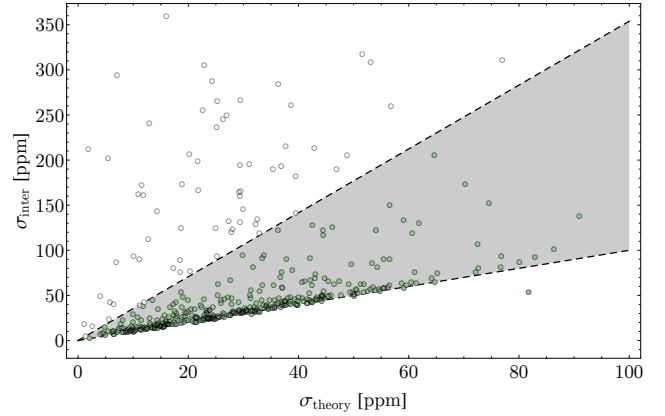


**Figure 4.** Scatter plot of the observed standard deviation versus the theoretical prediction with perfect detrending for the 477 KOIs considered in this work. Objects south of a ratio of 3.6 (upper dashed line) are considered to be of acceptable quality in what follows.

other and display a small spread. If the spread were large, this would indicate we have poorly selected our offset terms. Formally, rather than spread the standard deviation, we really want to minimize the chi-squared of the  $n_{\text{KOI}}$  points away from the average;  $\chi_j^2$ . Since we can do this for each and every binned phase point ( $n_{\text{bins}} = 450$  in total), the final cost function is the sum of all of these chi-squared terms i.e.  $C = \sum_{j=1}^{n_{\text{bins}}} (\chi_j^2)^2$ . In principle then, we simply need to minimize  $C$  with respect to  $n_{\text{KOI}}$  offset parameters, which we may write as

$$C(\theta) = \sum_{j=1}^{n_{\text{bins}}} \sum_{i=1}^{n_{\text{KOI}}} \left( \frac{(f_j^i - \theta^i) - \mu_j}{\sigma_j^i} \right)^2, \quad (12)$$

where we use  $i$  superscript to denote the  $i^{\text{th}}$  KOI and  $j$  subscript to denote the  $j^{\text{th}}$  binned phase point, and we further define  $\theta^i$  as the offset term associated with the  $i^{\text{th}}$  KOI, and  $\mu_j$  as the average of the  $j^{\text{th}}$  binned phase point.

One complication is that within each grand bin point, we want the points to lie close to the “average”,  $\mu_j$ , but we can again choose to define average in several different ways: a) simple mean b) weighted mean c) simple median d) weighted median. Between KOIs, the data is certainly heteroscedastic here and thus one should not expect the unweighted versions to be optimal. Nevertheless, we tried all four strategies on each planet group considered. We defined the preferred method as that which leads to the lowest median absolute deviation in the final grand stacked phase curve. For all planet groups considered, we found that the weighted mean was indeed the preferred metric, such that

$$\mu_j = \frac{\sum_{i=1}^{n_{\text{KOI}}} (f_j^i - \theta^i)(\sigma_j^i)^{-2}}{\sum_{i=1}^{n_{\text{KOI}}} (\sigma_j^i)^{-2}}. \quad (13)$$

Finally, we point out that for  $\sigma_j^i$ , we assume that for a particular given KOI, the errors are homoscedastic (although heteroscedastic across different KOIs) such that  $\sigma_j^i = \sigma^i$  for

all  $j = 1, 2, \dots, n_{\text{bins}} - 1, n_{\text{bins}}$ . Specifically, we set  $\sigma^i$  to be equal to the standard deviation of the residuals of each KOI's phase curve after an initial simple fit (as described earlier in Section 2.6), such that  $\sigma^i$  is equal to  $\sigma_{\text{inter}}$  of the  $i^{\text{th}}$  KOI. An illustration of this offset optimization scheme can be seen in Figure 5.

The uncertainty on the binned points is defined by  $1.4826^1$  multiplied by the median absolute deviation (MAD) of the final binned ensemble curve, after excluding phase points interior to within 5% of the orbital period centered on the transit. We opt to use the MAD as it is more robust against outliers than the typical standard deviation.

As a brief aside, the optimization of  $C$  is non-trivial due to the large dimensionality and non-linearity of the problem. To solve this, we initially set the vector of offset terms,  $\theta$ , to be zero and computed  $C(\theta)$ . We then replaced the first term,  $\theta^1$ , with a variable  $x$  and performed a simple downhill 1D minimization of  $C(\theta)$  with respect to  $x$ . We then replaced  $\theta^1$  with this optimal value and sequentially repeated for all elements of  $\theta$ . After completion, we saved the new  $C$  and then repeated the entire process again. This was done multiple times and we found rapid convergence of  $C$  to machine precision after just a few full iterative rounds.

## 2.8 Defining planet samples

The objective of this work is to measure the reflection component of the phase curve for a co-added sample of KOIs. Since phase curves are comprised of several other effects besides reflection, it is desirable to choose a subset for which these other effects are expected to have relatively little contribution. However, the amplitudes of each component are, a-priori, unknown to us although they can be predicted using empirically calibrated models.

To this end, we forecasted the amplitude of the ellipsoidal variations  $A_{\text{ellip}}$ , the beaming effect  $A_{\text{beam}}$ , the thermal component  $A_{\text{thml}}$ , and the reflection phase curve  $A_{\text{refl}}$  for each and every KOI. First, we obtained the posterior distributions for each planet's observed radius and forecasted mass from the study of [Chen et al. \(2018\)](#). The radius posteriors come from combining the [Mathur et al. \(2017\)](#) stellar posteriors and the [Rowe & Thompson \(2015\)](#) transit parameter posteriors together, whereas the forecasted masses come from the `forecaster` package ([Chen et al. 2017](#)). We then computed the forecasted beaming, ellipsoidal, reflection and thermal components. For all calculations, we assume zero eccentricity for simplicity.

For the beaming amplitude, we use Equation 9 of [Mazeh & Faigler \(2010\)](#), such that

$$A_{\text{beam}} = 4\alpha_{\text{beam}} \frac{K}{c}, \quad (14)$$

where  $K$  is the forecasted radial velocity amplitude, which can be computed from the forecasted planetary mass,  $c$  is the speed of light in a vacuum and  $\alpha_{\text{beam}}$  is a factor of order unity to account for the finite bandpass used and the

Doppler boosting effect by the spectrum shifting in and out of said bandpass ([Loeb & Gaudi 2003](#)). For this factor, we computed  $\alpha_{\text{beam}}$  using the IDL code of `alpha_beam` by Brian Jackson (private communication) which depends upon a single input, the effective temperature of the parent star. We computed  $\alpha_{\text{beam}}$  across a grid from 3000 K to 10000 K using the *Kepler* bandpass and found that a fourth-order polynomial - which is substantially faster to call - provides an excellent approximation, such that

$$\alpha_{\text{beam}} \simeq (7.89) + (-2.64 \times 10^{-3})T_{\text{eff}} + (4.33 \times 10^{-7})T_{\text{eff}}^2 + (-3.46 \times 10^{-11})T_{\text{eff}}^3 + (1.07 \times 10^{-15})T_{\text{eff}}^4. \quad (15)$$

For the ellipsoidal variations, we adopt Equation 7 of [Mazeh & Faigler \(2010\)](#), which is based upon the approximation of [Morris & Naftilan \(1993\)](#), such that

$$A_{\text{ellip}} = \alpha_{\text{ellip}} \frac{M_P}{M_\star} \left( \frac{R_\star}{a} \right)^3, \quad (16)$$

where  $\alpha_{\text{ellip}}$  is a coefficient well-approximated by

$$\alpha_{\text{ellip}} = 0.15 \frac{(15+u)(1+g)}{3-u}, \quad (17)$$

where  $u$  is the linear limb darkening coefficient and  $g$  is the stellar gravity darkening coefficient. For these coefficients, we queried the theoretical tabulation presented in [Claret & Bloemen \(2011\)](#) for the *Kepler* bandpass given a vector of inputs defined by  $\{T_{\text{eff}}, \log g, [\text{Fe}/\text{H}]\}$ . In order to draw intermediate points not present in the table, we trained a random forest interpolative algorithm on the three inputs, enabling us to quickly interpolate  $\alpha_{\text{ellip}}$  for any given choice of inputs.

For the reflection and thermal components, we adopt a fairly conservative choice for the geometric albedo equal to  $A_g = 0.1$ . Assuming a Lambertian sphere, this sets the Bond albedo to  $A_b = \frac{3}{2}A_g$ . We computed the day- and night-side temperatures of the planet using the prescription of [Cowan & Agol \(2011b\)](#), such that

$$T_{\text{day}} = T_0(1 - A_b)^{1/4} \left( \frac{2}{3} - \frac{5}{12}\beta \right)^{1/4}, \quad (18)$$

$$T_{\text{night}} = T_0(1 - A_b)^{1/4} \left( \frac{1}{4}\beta \right)^{1/4}, \quad (19)$$

where  $T_0$  is the temperature of the planet at the sub-stellar point ([Hansen 2008](#)), given by

$$T_0 \equiv T_{\text{eff}}(a/R_\star)^{-1/2}. \quad (20)$$

The  $\beta$  term here represents a redistribution factor that we set to  $\beta = \frac{1}{3}$ , as a low but not unreasonable value in order to maximize the thermal component of the phase curve. The thermal component was found by numerically integrating a linearly interpolated high-resolution tabulation of the *Kepler* bandpass multiplied by the Planck function for the planetary and stellar components respectively, and then taking the ratio multiplied by the ratio-of-radii squared. The flux-ratio integration is time consuming ( $\sim 0.1$  seconds per call) and given the large number of calls needed ( $\sim 20$  million) we decided to create an initial library of results from  $T_{\text{eff}} = 2000 \rightarrow 10000$  K and  $T_P = 300 \rightarrow 4000$  K on 30 K steps, which we then bicubic-spline interpolated later during the

<sup>1</sup> The 1.4826 value is a known scaling factor on the median absolute deviation (MAD) of a normal distribution that is needed in order to use the MAD as an estimate of the typical standard deviation ([Huber 1981](#)).



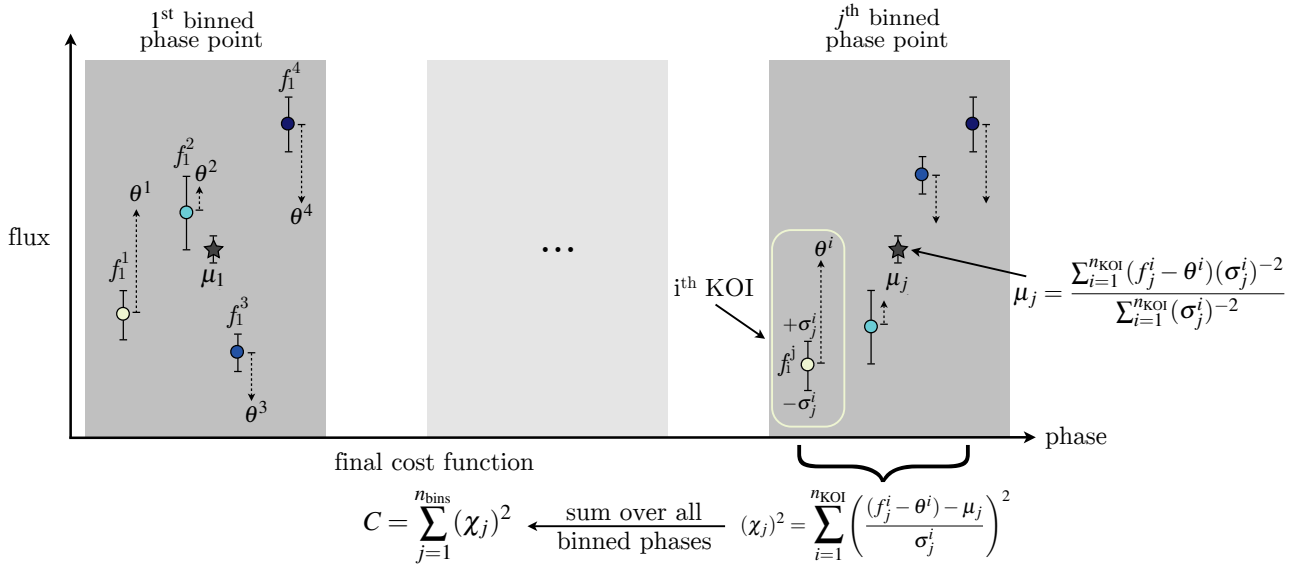


**Figure 5.** Illustration of the offset optimization scheme used between KOIs. Each KOI’s phase curve is offset by a constant  $\Theta^i$  for the  $i^{\text{th}}$  KOI, which is then optimized for by minimizing the cost function  $C$  depicted.

actual calculations on the posterior samples. Since we use a bicubic grid, we increased the edges of the grid by  $3^2$  grid points either side of our formal interpolation range to avoid boundary errors.

Finally, the reflection component is simply computed as  $A_{\text{refl}} = A_g p^2 (a/R_*)^{-2}$ , where  $p^2$  is the normalized transit depth. For each KOI, we step through the 40,000 joint posterior samples from [Chen et al. \(2018\)](#) and compute the corresponding set of phase curve amplitudes at each step. For each KOI, we also have a classification probability (Terran, Neptunian, Jovian or Stellar) based off the posteriors and **forecaster** prediction of [Chen et al. \(2018\)](#). These classifications are illustrated in Figure 6 for our KOIs under consideration.

We first defined a sample of sub-Jovians by using the **forecaster** classifications for which there is a  $\geq 90\%$  probability of the KOI being either Terran or Neptunian. Of these, we then split into Terran and Neptunian lists if the corresponding class probability exceeded 50%. For each KOI, we inspected the posterior samples of the forecasted  $A_{\text{refl}}$  and  $A_{\text{thml}}$  and counted the fraction of samples for which  $A_{\text{refl}} > 10^{1/2} A_{\text{thml}}$ . If this fraction exceeded 90%, we denote the planet as a “cool” KOI. Similarly, we counted the fraction of samples for which  $(A_{\text{refl}} + A_{\text{thml}}) > 10^{1/2} \max[A_{\text{beam}}, A_{\text{ellp}}]$  and those exceeding 90% fractions were labeled as “light” KOIs.<sup>2</sup> The final label we considered were KOIs for which we attribute the noise properties as most likely belonging to the quiet- or slow-like KIC samples; objects which for simplicity we dub as “quiet” (see Section 2.6 for details). Finally, we inspect the phase curves of each KOI by eye and exclude any which vary obviously from the overall sample.

We briefly highlight that we make no effort to account for or exclude KOIs with transit timing variations (TTVs).

<sup>2</sup> We use  $10^{1/2}$  because it is half an order-of-magnitude, and therefore becomes an order-of-magnitude when adding components in quadrature.

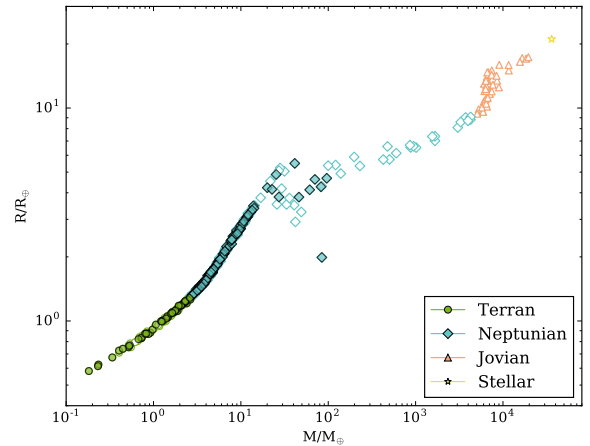


**Figure 6.** Classifications of each KOI using **forecaster** taken from [Chen et al. \(2018\)](#) for the 477 initial KOIs considered in this work. Classifications shown represent the modal class probability. Filled points were assigned as being “cool”, “quiet” and “light” (see Section 2.8 for explanation of these terms), as well as having a  $< 10\%$  chance of being Jovian or Stellar.

Short-period planets such as ours rarely exhibit TTVs and those that do are typically sufficiently low-amplitude to have negligible effect on the results presented here ([Mazeh et al. 2013](#)).

In total, our filters give us 115 quiet, light, cool Neptunians and 50 quiet, light, cool Terrans. For comparison with previously studied samples, we plot the size and equilibrium temperature of our sample in Figure 7.

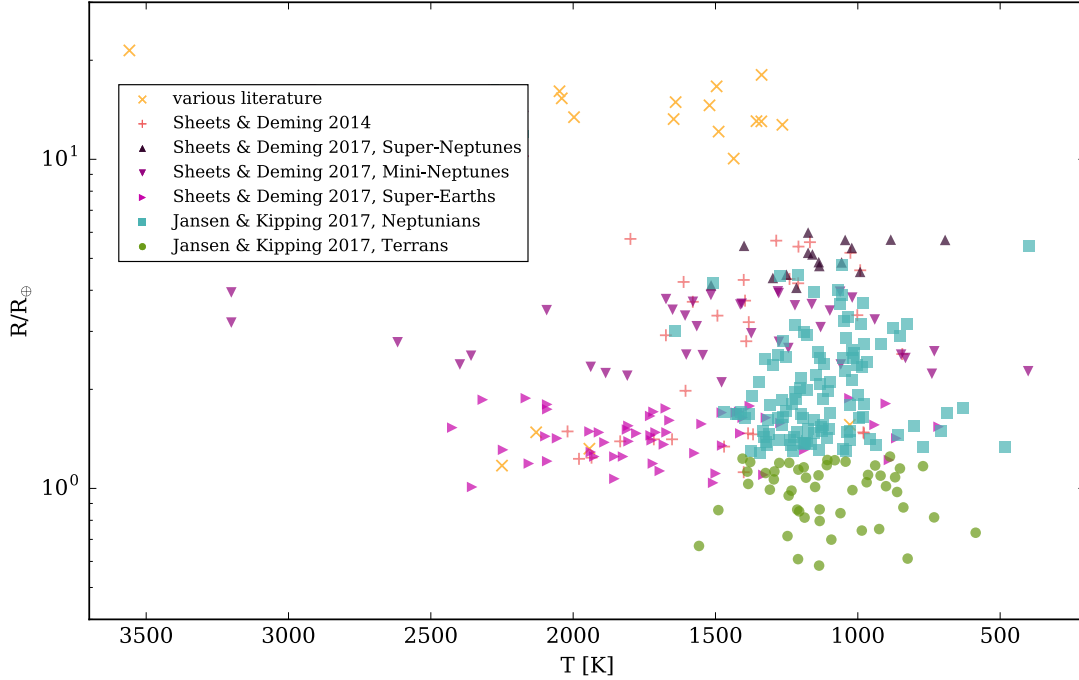


**Figure 7.** Illustrative comparison of our Terran and Neptunian sample versus that from [Sheets & Deming \(2014\)](#) and [Sheets & Deming \(2017\)](#), as well as other literature sources ([Désert et al. 2011](#); [Santerne et al. 2011](#); [Fortney et al. 2011](#); [Batalha et al. 2011](#); [Demory et al. 2011](#); [Esteves et al. 2013](#); [Sanchis-Ojeda et al. 2013](#); [Shporer et al. 2014](#); [Deleuil et al. 2014](#); [Demory 2014](#); [Gandolfi et al. 2015](#); [Angerhausen et al. 2015](#); [Armstrong et al. 2016](#))

### 3 FORWARD MODEL

To measure the representative reflection and thermal quantities of the ensembles, we first generate model phase curves from the sum of a reflection component and a thermal component. The reflection component is assumed to be symmetric for the ensemble, and is proportional to the Bond albedo  $A_B$  under the Lambertian approximation. The thermal component then depends on the thermal redistribution efficiency factor  $\varepsilon$  and the greenhouse factor  $f$ .

The thermal redistribution efficiency is here defined to be the ratio between the radiative timescale of the planet’s photosphere and the difference between the frequencies at which the photosphere rotates about the planet and the surface rotates about its axis. In other words, if the atmospheric mass heated at the substellar point is redistributed about the surface much faster than the heat gets reradiated, the planet would be described as having a large redistribution efficiency  $\varepsilon$ , typically  $\varepsilon \gg 1$ . Conversely, a planet with relatively no heat redistribution would be described as having  $\varepsilon = 0$ . For a planet which has winds moving in a direction opposite of the planetary rotation,  $\varepsilon$  is defined to be negative. The greenhouse factor  $f$  is simply a scaling factor which accounts for any temperature boost due to the presence of greenhouse gases in the atmosphere.

Our model described in the following section allows us to compute the phase curve of a single exoplanet accounting for thermal emission and reflection. However, as described in Section 2, the final data product under analysis is an ensemble

of many exoplanets. In what follows, we will assume that each planet within a subset shares the same Bond albedo,  $A_B$ , thermal redistribution factor,  $\varepsilon$  and greenhouse factor,  $f$ . These parameter inferences should be interpreted as measurements of the “typical” or “representative” values, since in reality there will be an underlying and unknown distribution of these terms.

#### 3.1 Thermal component

We express the thermal emission component of the normalized planetary flux as

$$F_T = \frac{1}{\pi B_{K,\star}} \left( \frac{R_P}{R_\star} \right)^2 \times \int_{-\frac{\pi}{2}}^{\frac{\pi}{2}} \int_{-\frac{\pi}{2}}^{\frac{\pi}{2}} B_{K,P}[T(\alpha, \theta, \phi)] \cos^2 \theta \cos \phi d\theta d\phi \quad (21)$$

where  $B_{K,\star}$  is the Planck function of the host star convolved with the Kepler bandpass,  $R_P$  is the radius of the planet,  $R_\star$  the radius of the star, and  $B_{K,P}[T(\alpha, \theta, \phi)]$  is the temperature distribution-dependent blackbody curve of the planet convolved with the Kepler bandpass,

$$B_{K,P}[T(\alpha, \theta, \phi)] = \int_{\lambda} K_{\lambda} \frac{2hc^2}{\lambda^5} \times \left[ \exp \left( \frac{hc}{\lambda k_B T(\alpha, \theta, \phi)} \right) - 1 \right]^{-1} d\lambda \quad (22)$$

where  $K_\lambda$  is the Kepler response function,  $T(\alpha, \theta, \phi)$  is the phase-dependent temperature distribution across the planet's surface, and where  $\alpha$ ,  $\theta$  and  $\phi$  represent the planetary phase, latitude and longitude as viewed in the observer's frame of reference, respectively. For our models we have chosen a surface resolution of  $15^\circ \times 15^\circ$  in latitude and longitude, where further increasing the resolution changes the thermal amplitude on the order of one-hundredth of a percent. It should be noted that  $\phi$  and  $\theta$  are independent of phase, where  $\phi \equiv 0$  in the direction of the observer.

We borrow from [Hu et al. \(2015\)](#) to define the phase-dependent temperature distribution  $T(\alpha, \theta, \phi)$  to be equal to

$$T(\alpha, \theta, \phi) = fT_0(\theta)\mathcal{P}(\varepsilon, \xi) \quad (23)$$

where  $f$  is the greenhouse boosting factor,  $T_0$  is the sub-stellar temperature, and  $\mathcal{P}$  is the thermal phase function, which for a planet on a circular orbit can be expressed by Equation (10) in [Cowan & Agol \(2011\)](#):

$$\frac{d\mathcal{P}}{d\xi} = \frac{1}{\varepsilon}(\max(\cos \xi, 0) - \mathcal{P}^4) \quad (24)$$

where  $\max(\cos \xi, 0) = \frac{1}{2}(\cos \xi + |\cos \xi|)$ , i.e. a cosine function truncated at negative values. We borrow our notation from [Hu et al. \(2015\)](#), where  $\xi$  represents the local planetary longitude defined for all points in phase to be  $\xi \equiv \phi - \alpha$ . The phase term  $\alpha$  ranges from  $-\pi$  to  $\pi$  and is defined to be zero at the secondary eclipse. For a planet with prograde rotation,  $\xi = 0$  at the sub-stellar longitude,  $\xi = -\pi/2$  at the dawn terminator, and  $\xi = \pi/2$  at the dusk terminator.

Equation (24) does not have an analytic solution, so we solve it numerically using `scipy`'s ODE integrator, where we set the initial conditions equal to the approximated expression for  $\mathcal{P}_{\text{dawn}}$  stated in the Appendix of [Cowan & Agol \(2011\)](#),

$$\mathcal{P}_{\text{dawn}} \approx \left[ \pi + (3\pi/\varepsilon)^{4/3} \right]^{-1/4}. \quad (25)$$

The sub-stellar temperature as a function of planetary latitude  $\theta$  is expressed by

$$T_0(\theta) = T_\star \left( \frac{R_\star}{a} \right)^{1/2} (1 - A_B)^{1/4} \cos \theta^{1/4} \quad (26)$$

where  $T_\star$  is the effective temperature of the host star and  $a$  the semi-major axis.

### 3.2 Reflection component

The reflection component of the phase curve is given by

$$F_R = \left( \frac{R_p}{a} \right)^2 \frac{2}{3} A_B \frac{1}{\pi} [\sin |\alpha| + (\pi - |\alpha|) \cos |\alpha|] \quad (27)$$

where we adopt the Lambertian approximation so that  $A_B = \frac{3}{2} A_g$ . According to [Seager et al. \(2000\)](#) and [Cahoy et al. \(2010\)](#), this is a fine approximation under the homogeneously reflecting atmosphere assumption.

## 4 REGRESSION

### 4.1 Constructing a likelihood

To infer a subset's atmospheric parameters  $A_B$ ,  $\varepsilon$ , and  $f$ , we require a likelihood function to describe the probability of

obtaining the ensemble data given a particular realization of an ensemble model. To create an ensemble model for a particular choice of the atmospheric properties,  $F_{\text{tot}}(A_B, \varepsilon, f)$ , we first generate the phase curves of each individual planet using a set of global atmospheric parameters, denoted by  $F_{i,\text{tot}}(A_B, \varepsilon, f)$  where  $i$  is the planet index. We next take the weighted average of the individual phase curves using the same weighting as that used for the real data stacking (see Section 2.7). Finally, this ensemble model is then subtracted from the ensemble data to calculate the residuals,  $r_i$ . With the residuals in hand, we write a likelihood function by assuming that the ensemble data points are independent and normally distributed, such that

$$\log \mathcal{L} = - \sum_{i=1}^N \frac{1}{2} \log(2\pi) - \sum_{i=1}^N \log \sigma_i - \frac{1}{2} \sum_{i=1}^N \left( \frac{r_i}{\sigma_i} \right)^2. \quad (28)$$

We make two modifications to our model beyond that described thus far. First, we allow our likelihood function to account for the possibility of underestimated uncertainties. Recall that the measurement uncertainties on each binned point are computed using the median absolute deviation yet we acknowledge the possibility that these may underestimate the true value. We therefore add a "jitter" term,  $\sigma_{\text{jitter}}$ , in quadrature to the errors, which is itself treated as a free parameter in the model, similar to the prescription described by [Teachey et al. \(2018\)](#). Second, although our data has been carefully normalized and offset (see Section 2.7), we include an offset term to the final ensemble as a free parameter,  $\gamma$ , which simply allows us to propagate the uncertainty of the offset into the covariances of any resulting posteriors and serve as a final check that the data are indeed normalized correctly.

### 4.2 Model Look-Up Tables (LUTs)

In practice, we found that calling our PYTHON implementation of the phase curve model for each planet at each phase point was sufficiently computationally expensive to make conventional Bayesian regression too time consuming. To solve this, we elected to build a pre-computed look-up table (LUT) of ensemble model phase curves across a three-dimensional grid of  $A_B$ ,  $\varepsilon$  and  $f$ . For any given choice of these parameters, we can then conduct a tri-linear interpolation of the regular grid to reproduce any choice we wish that falls within the LUT's calibrated range.

The ensemble models take into account the uncertainties in the measurements of stellar radius, mass, effective temperature, and density by sampling from corresponding posterior distributions of these quantities given in [Mathur et al. \(2017\)](#), generating model phase curves from each sample draw, then implementing the average of these phase curves.

The parameter space from which we generate the models spans a uniform range of  $A_B$  from  $[0.0, 1.0]$  at a resolution of  $\Delta A_B = 0.01$ ,  $f$  from  $[1.0, 2.0]$  at a resolution of  $\Delta f = 0.1$ , and a log uniform range of  $\log \varepsilon$  from  $[-1.7, 1.7]$  at a resolution of  $\Delta \log \varepsilon = 0.05$ . It is possible for the redistribution factor to extend beyond these limits to infinity, however we consider the change in the thermal component for  $|\varepsilon| > 50$  to be negligible.

### 4.3 Bayesian regression and priors

We utilize `emcee` (Foreman-Mackey et al. 2013) to perform an Affine Invariant Markov chain Monte Carlo (MCMC) procedure on the ensemble phase curves. We obtain  $2 \times 10^6$  samples using 100 walkers, burning the first half of the chain for a remaining total of  $10^6$  samples. Our priors span a uniform range of  $A_B$  from  $[0.0, 1.0]$ ,  $f$  from  $[1.0, 2.0]$ , and  $\epsilon$  from  $[-50, 50]$ . Although we generated the models spanning a log-uniform range of  $\epsilon$ , sampling from a uniform prior distribution is sufficient for this parameter due to its low impact on the model at  $\epsilon \gtrsim 10$ .

### 4.4 Savage-Dickey density ratio (SDDR)

For a model which contains all of the parameters of another plus at least one additional parameter, Dickey & Lientz (1970) show that the Bayes factor between the nested model and its parent model can be estimated by simply taking the ratio of the probability density of the full model at the null point of the nested model to the prior distribution at that same point, also known as the Savage-Dickey density ratio (SDDR).

For the purpose of completeness, we use the SDDR to compare the results of a fit to a “black planet” model (i.e.  $A_B = 0$ ) to the results of the fit to the full reflection-thermal model. Because the black-planet model is a nested case of the full model, computing the SDDR is an appropriate method of odds comparison for these models. Further, since the black-planet model is separated by just one free parameter from the full model, the density of samples is sufficiently high to accurately resolve the SDDR.

For a probability density  $\mathcal{P}$  and uniform prior distribution of the full model  $\Pi_{\text{full}}$ , we can estimate the Bayes factor with the SDDR to be

$$B_{\text{black:full}} = \frac{\mathcal{P}_{\text{full}}(A_B = 0)}{\Pi_{\text{full}}(A_B = 0)}. \quad (29)$$

## 5 RESULTS

### 5.1 Terran ensemble

Our model accounts for both the thermal and reflected light component of an exoplanetary phase curve, and there is a certain degree of trade-off between the two. This degeneracy means that low signal-to-noise phase curves, as might be expected for small planets, can have marginalized posterior distributions for albedo and greenhouse factor which, when taken independently, appear consistent with zero and thus a null detection. Accordingly, when considering the basic question as to whether any kind of signal is detected or not, inspection of marginalized one-dimensional model parameter posteriors is not the most robust tool. Instead, we argue that it is better to compute the amplitude of the phase curve directly at each posterior sample and then construct an a-posteriori amplitude distribution when evaluating detection significance. Since the phase curve model is non-sinusoidal, a simple amplitude estimate is not directly available, but we can easily compute the root mean square (RMS) amplitude of any given phase curve model, which is suitable as a proxy for signal amplitude.

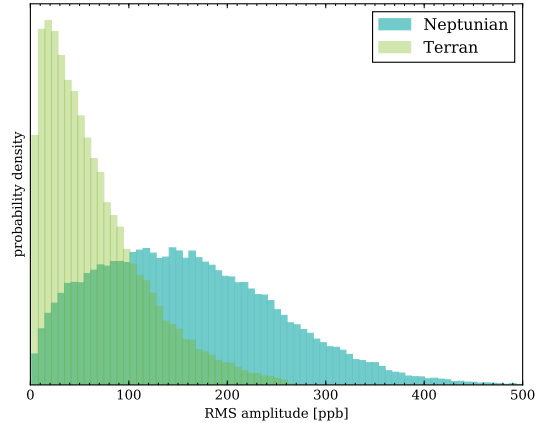


**Figure 8.** Posterior distributions of the root mean square amplitudes for the Neptunian and Terran ensemble data. The fit to the Terran ensemble returns an upper limit on the RMS amplitude of 169 parts per billion to the 95% confidence level, while the fit to the Neptunian ensemble returns an RMS amplitude of  $150^{+100}_{-90}$  parts per billion.

The RMS amplitude posterior for the Terran worlds, shown in Figure 8, shows no strong offset from zero and thus appears compatible with a null detection. Taking the median and surrounding 68.3% quantile, the amplitude is measured to be  $53^{+60}_{-40}$  parts per billion - a remarkably precise photometric precision even by *Kepler*’s standards. As a result, we treat the albedo and greenhouse factor, model parameters which are degenerate yet control amplitude, as also being null detections. These null detections are corroborated by peaks in the posterior distributions at  $A_B = 0$  and  $f = 1$ .

From our posteriors we instead measure an upper limit on the Bond albedo of  $A_B < 0.63$  to 95% confidence, which under the Lambertian assumption of our model, corresponds to an upper limit on the geometric albedo of  $A_g < 0.42$ . Similarly, we measure an upper limit on the greenhouse factor of  $f < 1.6$  to 95% confidence, and we find that the thermal redistribution factor remains unconstrained. As expected, the vertical offset  $\gamma$  and error correction  $\sigma_{\text{jitter}}$  terms are marginal. The posterior distributions for the fit to the model can be seen in Figure 9.

The posterior distribution of  $\epsilon$  displays a non-uniform shape despite using a uniform prior. The complex interplay of this parameter with the other model parameters meant we did not have full conviction that this posterior was not simply a general artifact of null detections. To test this, we scrambled the Terran phase curve data randomly in phase, and then re-fitted using the same algorithm. These posteriors, shown as black dashed lines in Figure 9, reveal that indeed the  $\epsilon$  posterior is an expected product of null detections and we give it little weight as a significant effect in what follows.

We briefly highlight that the posteriors from the real data display a more defined peak at  $A_B = 0$  than the scrambled data. Since the real data must contain a genuine signal at some level (even if formally undetectable), it is more likely to be coherent than scrambled data, potentially explaining



**Table 1. Terran results:** 68.3% credible intervals on the posterior distributions for our model parameters. Upper panel lists the actual model parameters used, whereas lower panel lists three other terms of interest.

parameter	real data	scrambled data
$A_B$	$0.18^{+0.24}_{-0.13}$	$0.3^{+0.3}_{-0.2}$
$f$	$1.3^{+0.2}_{-0.2}$	$1.3^{+0.3}_{-0.2}$
$\epsilon$	$-1^{+40}_{-30}$	$-5^{+40}_{-30}$
$\gamma$ [ppm]	$0.01^{+0.05}_{-0.01}$	$0.01^{+0.04}_{-0.01}$
$\sigma_{\text{jitter}}$ [ppm]	$0.47^{+0.08}_{-0.11}$	$0.5^{+0.1}_{-0.1}$
$A_g$	$0.12^{+0.16}_{-0.09}$	$0.20^{+0.22}_{-0.14}$
RMS [ppb]	$53^{+60}_{-40}$	$86^{+90}_{-60}$
$B(A_B = 0 : A_B > 0)$	3.35	1.96

**Table 2. Neptunian results:** 68.3% credible intervals on the posterior distributions for our model parameters. Upper panel lists the actual model parameters used, whereas lower panel lists three other terms of interest.

parameter	real data	scrambled data
$A_B$	$0.15^{+0.12}_{-0.10}$	$0.08^{+0.1}_{-0.06}$
$f$	$1.18^{+0.14}_{-0.12}$	$1.18^{+0.14}_{-0.12}$
$\epsilon$	$-6^{+40}_{-30}$	$-7^{+40}_{-30}$
$\gamma$ [ppm]	$0.01^{+0.05}_{-0.01}$	$0.01^{+0.06}_{-0.01}$
$\sigma_{\text{jitter}}$ [ppm]	$0.14^{+0.23}_{-0.14}$	$0.17^{+0.21}_{-0.17}$
$A_g$	$0.10^{+0.08}_{-0.07}$	$0.06^{+0.07}_{-0.04}$
RMS [ppb]	$150^{+100}_{-90}$	$87^{+90}_{-60}$
$B(A_B = 0 : A_B > 0)$	2.77	6.46

this observation. However, it is not exactly clear why the scrambled data and the real data do not produce identical posteriors, but it is also not obvious what level of difference should be interpreted as meaningful either. Nonetheless, it does not affect the final interpretation that there is no compelling case for a detection.

As described in Section 4.4, we computed the Bayes factor between the full model and a simpler black-planet model where we fix  $A_B = 0$ . This reveals a slight preference for the simpler model than the more general case ( $B_{\text{black:full}} = 3.35$ ), which is consistent with the result expected from a null result.

All of the measured and derived values for the fit to the Terran ensemble data can be seen in Table 1.

## 5.2 Neptunian ensemble

For the Neptunian ensemble, we again computed a posterior distribution for the RMS phase curve amplitude and find it peaks somewhat away from zero, as can be seen in Figure 8, giving  $150^{+100}_{-90}$  ppb. To estimate the significance, we use the Lucy & Sweeney (1971) test to derive a false alarm probability of 5.8% ( $1.9\sigma$ ). Accordingly, whilst certainly intriguing,

we do not consider this to be a significant “detection” and thus treat the inferred albedo and greenhouse factor parameters as upper limits, as with the Terran sample.

From the marginalized posteriors, we derived an upper limit on the ensemble Neptunian Bond albedo of  $A_B < 0.35$  to 95% confidence, or  $A_g < 0.23$  when converted to a geometric albedo. As before, the thermal redistribution efficiency remains unconstrained but we can constrain the greenhouse factor to be  $f < 1.40$  to 95% confidence. The posterior distributions of the fit to the full thermal-reflection model can be seen in Figure 10. The vertical offset  $\gamma$  and error correction  $\sigma_{\text{jitter}}$  terms are again marginal.

Comparing the posterior distributions of the full fit to the data to that of the fit to the scrambled in Figure 10 shows that they are nearly identical for all parameters except for the Bond albedo. Here, the scrambled data produces a posterior peaked at zero whereas the real data prefer a slightly positive value, consistent with tentative evidence for a detection found from the RMS amplitude posterior. Despite the posterior distribution of the thermal redistribution efficiency showing a preference for negative values (i.e. subrotating winds), this behavior is also displayed by the fit to the scrambled data, which again suggests that this is not significant.

The Bayes factor as estimated by the Savage-Dickey ratio for the true Neptunian ensemble data is determined to be  $B_{\text{black:full}} = 2.77$ , which suggests that there is no substantial evidence for a preference for the black-planet model over the full model. The weak preference of the black-planet model over the full model can be corresponded to a  $1.1\sigma$  significance ( $\sqrt{2}\text{erfc}^{-1}[1/(B+1)]$ ; see Kipping et al. 2010). We note however that the degree to which the black planet model is favored is less than that of the scrambled data, the opposite to what happened with the definitively null detection of the Terran ensemble.

All of the measured and derived values for the fit to the Neptunian ensemble data can be seen in Table 2.

We briefly comment that inspection of Figure 10 reveals a suggestive transit-like feature at around  $-0.25$  phase. We conducted a nonlinear least squares regression of a box-like dip seeding from around this phase and achieved a  $\chi^2$  improvement of 14.1 versus a flat-line. Given that three extra free parameters are necessary (a mid-time, a depth and a duration), this improvement does not outweigh the likelihood penalty from the Schwarz (1978) BIC criterion ( $3\log 450 = 18.3$ ) and thus we do not consider it to be significant.

To ensure this feature does not significantly skew our results, we removed the points between phases  $-0.26$  and  $-0.18$  and repeated our fits from earlier. Referencing the results in Table 3, we find that the maximum a-posteriori values change by less than one-sigma and thus this feature does not appear to significantly affect our inferences. Naturally, when conditioning our inferences upon this truncated data set the upper limits described earlier tend to be slightly modified, with a 95% confidence upper limit on the Bond albedo of  $A_B < 0.26$ , or  $A_g < 0.17$  when converted to geometric albedo. As with the full set of data, the thermal redistribution efficiency remains unconstrained, while an upper limit on the greenhouse factor is constrained to  $f < 1.47$  to 95% confidence.

**Table 3. Results of the Neptunian phase curve minus points of interest:** 68.3% credible intervals on the posterior distributions for our model parameters on the Neptunian ensemble with points between phases -0.26 and -0.18 removed. Upper panel lists the actual model parameters used, whereas lower panel lists three other terms of interest.

parameter	real data	scrambled data
$A_B$	$0.07^{+0.1}_{-0.06}$	$0.11^{+0.07}_{-0.09}$
$f$	$1.26^{+0.15}_{-0.18}$	$1.25^{+0.15}_{-0.16}$
$\epsilon$	$8^{+30}_{-40}$	$-5^{+40}_{-30}$
$\gamma$ [ppm]	$0.02^{+0.14}_{-0.02}$	$0.02^{+0.13}_{-0.02}$
$\sigma_{\text{jitter}}$ [ppm]	$0.09^{+0.3}_{-0.09}$	$0.09^{+0.3}_{-0.04}$
$A_g$	$0.05^{+0.07}_{-0.04}$	$0.07^{+0.05}_{-0.06}$
RMS [ppb]	$78^{+80}_{-50}$	$114^{+100}_{-70}$

## 6 DISCUSSION

In this work, we have produced the first demonstration of a population-stack of exoplanet phase curves for 50 Terran and 115 Neptunian confirmed *Kepler* planets. Enabling this analysis, we have devised a simple but powerful non-parametric detrending algorithm optimized for reconstructing the phase curves of transiting planets, dubbed **phasma**. A mathematical motivation, example test, and a battery of control cases are presented to justify our use of this new code.

After detrending, stacking and regressing ensemble phase curve models to our data product, we find modest evidence ( $2.4\sigma$ ) for a coherent signal in the 115-planet Neptunian sample, with an R.M.S. amplitude of  $150^{+100}_{-90}$  parts per *billion*. Given the weak significance of the signal and the covariances between atmospheric model parameters, the model parameters have greater fractional uncertainty, with the 68.3% credible interval on geometric albedo being  $A_g = 0.10^{+0.08}_{-0.07}$  for the Neptunian ensemble. This measurement peaks slightly further out than our fits on control-data without any signal, but we do not consider it significant enough to claim a detection. Accordingly, we use the posterior to derive an upper limit of  $A_g < 0.23$  to 95% confidence.

This result indicates that most of the Neptunians in our ensemble are significantly darker than Neptune, which has a full-disk albedo of 0.30 when integrated across the *Kepler* response function (using the albedo spectrum from Karkoschka 1994). Lower albedos for warm Neptunians has been predicted theoretically, as a consequence of temperatures becoming too warm for bright clouds to form (Cahoy et al. 2010). The increased insolation on these short-period planets can also lead to Doppler broadened spectral lines, for example of sodium and potassium, which can also contribute to a lower albedo (Sudarsky et al. 2000; Seager et al. 2000; Spiegel et al. 2010; Heng 2016).

Our result may be compared to the stacked occultation measurement of Sheets & Deming (2017), who find a typical geometric albedo of  $A_g = (0.05 \pm 0.04)$  and  $(0.11 \pm 0.06)$  for  $2-4 R_\oplus$  and  $4-6 R_\oplus$  *Kepler* planets, respectively. However, there are several important differences in the samples (some of these can be seen illustratively in Figure 7). First, our definition of a Neptunian planet, deduced by the classification algorithm **forecaster**, does not directly correspond to

the radius cut of  $2-6 R_\oplus$ , rather we extend down further to  $\sim 1.25 R_\oplus$ . Second, the Neptunian planets used in this work are all dispositioned as “CONFIRMED” rather than “CANDIDATE” on the NASA Exoplanet Archive. Finally, our sample is considerably cooler than the planets used by Sheets & Deming (2017), whose sample has a mean equilibrium temperature of  $\sim 2000$  K versus  $\sim 1200$  K for this work. Nevertheless, the results are broadly consistent and support a warm Neptunian albedo of  $A_g \lesssim 0.2$ .

For the 50-planet Terran sample, we have derived what appears to be the first measurement of this type of planet’s average albedo. Whilst Sheets & Deming (2017) do have a category dubbed “Super-Earths”, spanning  $1-2 R_\oplus$ , probabilistic classifications from **forecaster** (Chen et al. 2017) indicate that the majority of such planets are more likely to belong to a population with a mass-radius relation describing gaseous bodies, rather than solid ones. Aside from the predictions of **forecaster**, we highlight that other independent studies support the argument that a  $1-2 R_\oplus$  category would, at the very least, have significant contamination of mini-Neptunes within its sample (e.g. see Lopez & Fortney 2014; Rogers 2015; Lehmer 2017; Fulton et al. 2017).

Although our work derives the first Terran-ensemble albedo, the measurement is an upper limit rather than a detection, as with the Neptunian set. Specifically, we measure an upper limit on the representative geometric albedo of our 50-planet Terran ensemble to be  $A_g < 0.42$  to 95% confidence. This excludes a Venusian geometric albedo of 0.67 (i.e. planets covered in reflective clouds or hazes), as well as the less likely case of icy-covered surface such as Europa or Enceladus. However our measurement remains compatible with a Mercurian or Martian value (0.14 and 0.17 respectively; albedos taken from Mallama 2009).

With a mean temperature of  $\sim 1000$  K, the Terrans considered here are unlikely to be covered in lava-oceans, as has been hypothesized for ultra-short period *Kepler* planets (Rouan et al. 2011) and so these worlds are more likely to resemble Mercury. Aside from an albedo constraint, we also find that the null detection constrains the thermal component such that the marginalized greenhouse factor must be  $f < 1.60$  to the 95% confidence level. This result is inconsistent with a Venusian strong greenhouse, which together with the lower albedo adds weight to contention that our sample of Terran planets are likely non-Venusian in nature. This would be compatible with a lack of thick atmosphere as a product of photo-evaporative sculpting (Lehmer 2017), leaving behind a dark, basaltic surface (Hu et al. 2012).

Continued photometric surveys for transiting planets promises to greatly increase our sample of small planets suitable for analysis. The techniques described in this work show great promise to measure the albedo of larger samples of planets, even at longer orbital periods in the near future.

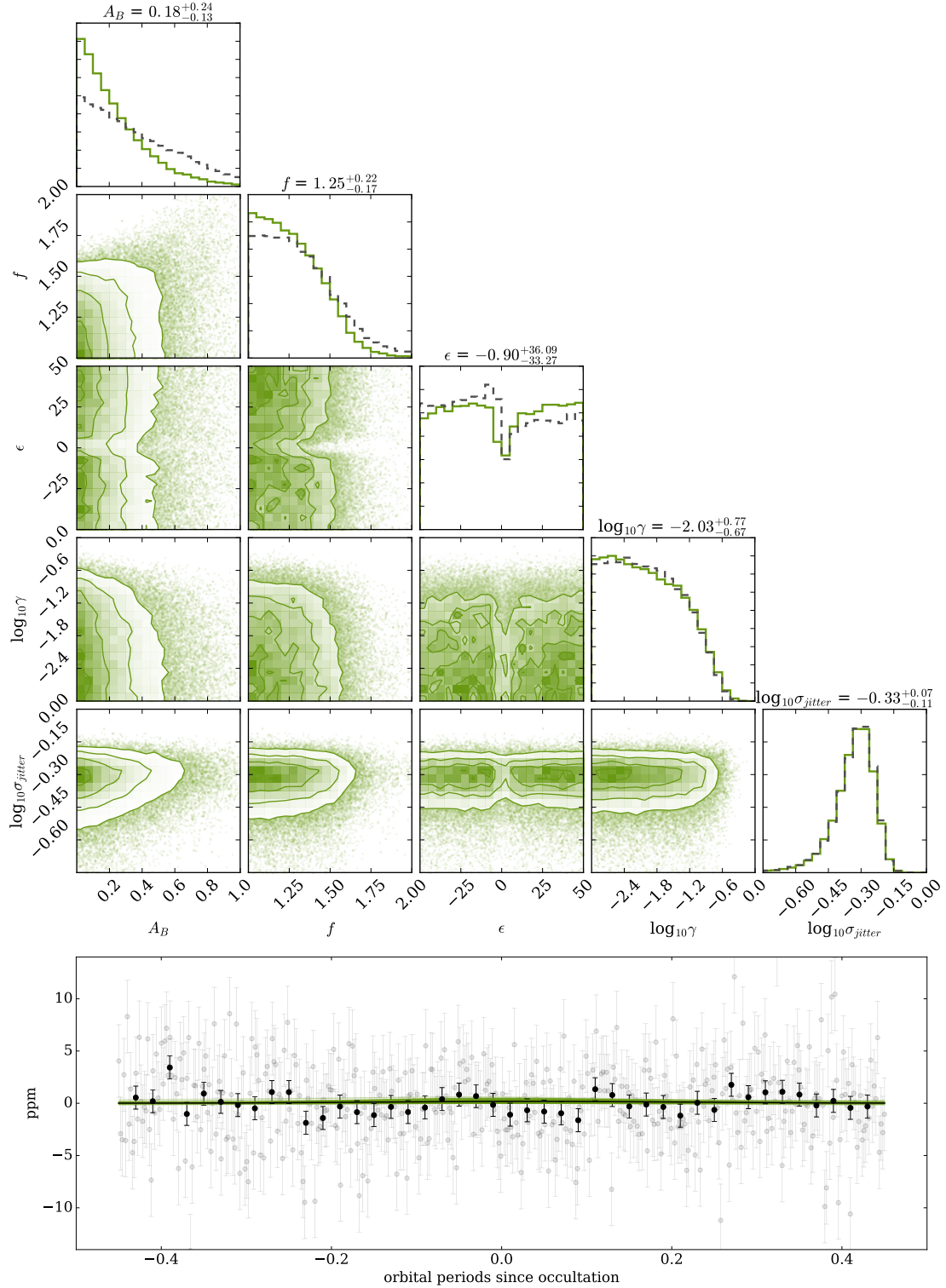


**Figure 9.** Posterior distributions of the full thermal-reflection model fit for the Terran ensemble, where the 1-D histograms show the probability densities of the fit to the ensemble data in solid-green and to the flat-line data in dashed-grey [top]. The bottom panel shows the binned ensemble data (500 bins in grey, 50 bins in black) plotted with model phase curves constructed from parameters sampled from the posterior distributions (green), where the median phase curve is overplotted in black.

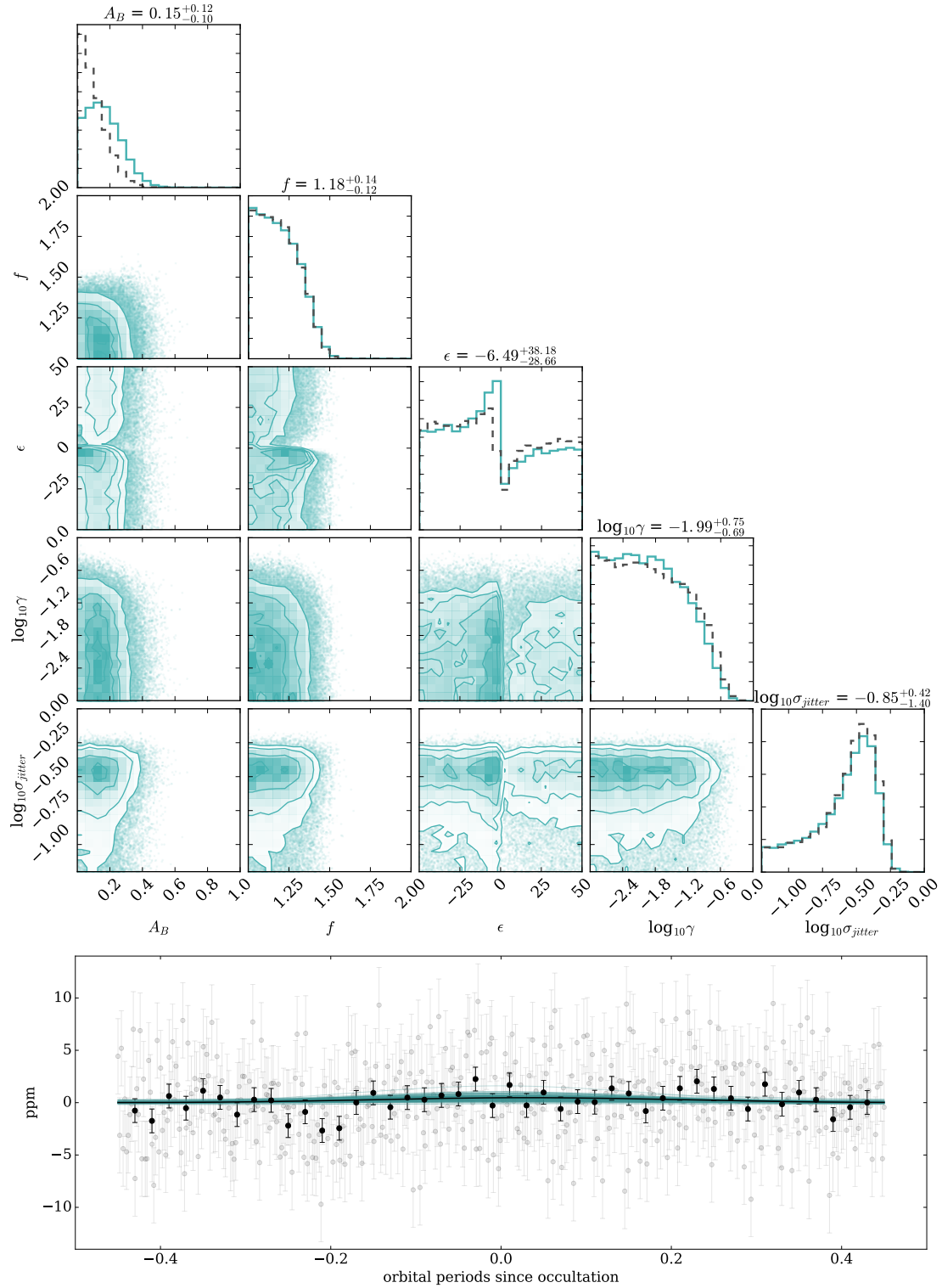


**Figure 10.** Posterior distributions of the full thermal-reflection model fit for the Neptunian ensemble, where the 1-D histograms show the probability densities of the fit to the ensemble data in solid-blue and to the flat-line data in dashed-grey [top]. The bottom panel shows the binned ensemble data (500 bins in grey, 50 bins in black) plotted with model phase curves constructed from parameters sampled from the posterior distributions (blue), where the median phase curve is overplotted in black.



## ACKNOWLEDGMENTS

This research has made use of the `forecaster` predictive package by [Chen et al. \(2017\)](#), the `corner.py` code and `emcee` package by Dan Foreman-Mackey at [github.com/dfm/corner.py](https://github.com/dfm/corner.py) and [github.com/dfm/emcee](https://github.com/dfm/emcee), `scipy`, `astropy`, and the NASA Exoplanet Archive, which is operated by the California Institute of Technology, under contract with the National Aeronautics and Space Administration under the Exoplanet Exploration Program.

Thanks to David Armstrong for sending us his team's HAT-P-7b detrended phase curve, and Brian Jackson for sharing his IDL code `alpha_beam`. We would also like to thank the reviewer for their helpful comments.

## REFERENCES

- Akeson, R. L., Chen, X., Ciardi, D., et al. 2013, *PASP*, 125, 989
- Angerhausen, D., DeLarme, E., Morse, J. A., 2015, *PASP*, 127, 1113
- Armstrong, D. J., de Mooij, E., Barstow, J., Osborn, H. P., Blake, J. & Fereshteh Saniee, N. 2016, *Nature Astronomy*, 1, 4
- Barclay, T., Huber, D., Rowe, J. F., Fortney, J. J., Morley, C. V., Quintana, E. V., Fabrycky, D. C., Barentsen, G., Bloemen, S., Christiansen, J. L., Demory, B.-O., Fulton, B. J., Jenkins, J. M., Mullally, F., Ragozzine, D., Seader, S. E., Shporer, A., Tenenbaum, P. & Thompson, S. E., 2012, *ApJ*, 761, 53
- Batalha, N. M., Borucki, W. J., Bryson, S. T., Buchhave, L. A., Caldwell, D. A., Christensen-Dalsgaard, J., Ciardi, D., Dunham, E. W., Fressin, F., Gautier, T. N., Gilliland, R. L., Haas, M. R., Howell, S. B., Jenkins, J. M., Kjeldsen, H., Koch, D. G., Latham, D. W., Lissauer, J. J., Marcy, G. W., Rowe, J. F., Sasselov, D. D., Seager, S., Steffen, J. H., Torres, G., Basri, G. S., Brown, T. M., Charbonneau, D., Christiansen, J., Clarke, B., Cochran, W. D., Dupree, A., Fabrycky, D. C., Fischer, D., Ford, E. B., Fortney, J., Girouard, F. R., Holman, M. J., Johnson, J. A., Isaacson, H., Klaus, T. C., Machalek, P., Moorehead, A. V., Morehead, R. C., Ragozzine, D., Tenenbaum, P., Twicken, J., Quinn, S., VanCleve, J., Walkowicz, L. M., Welsh, W. F., Devore, E. & Gould, A., 2011, *ApJ*, 729, 27
- Birkby, J. L., de Kok, R. J., Brogi, M., de Mooij, E. J. W., Schwarz, H., Albrecht, S. & Snellen, I. A. G., 2013, *MNRAS*, 436, 35
- Borucki, W. J., Koch, D., Jenkins, J., et al. 2009, *Science*, 325, 709
- Burrows, A. S., 2014, *Nature*, 513, 345
- Cahoy, K. L., Marley, M. S. & Fortney, J. J. 2010, *ApJ*, 724, 189
- Charbonneau, D., Brown, T. M., Noyes, R. W. & Gilliland, R. L. 2002, *ApJ*, 568, 377
- Charbonneau, D., Knutson, H. A., Barman, T., Allen, L. E., Mayor, M., Megeath, S. T., Queloz, D. & Udry, S., 2008, *ApJ*, 686, 1341
- Chen, J. & Kipping, D. M. 2017, *ApJ*, 834, 17
- Chen, J. & Kipping, D. M. 2018, *MNRAS*, 473, 2753
- Christiansen, J. L., Jenkins, J. M., Caldwell, D. A., Burke, C. J., Tenenbaum, P., Seader, S., Thompson, S. E., Barclay, T. S., Clarke, B. D., Li, J., Smith, J. C., Stumpe, M. C., Twicken, J. D., Van Cleve, J., 2013, *PASP*, 124, 1279
- Claret, A. & Bloemen, S. 2011, *A&A*, 529, 75
- Cowan, N. B., & Agol, E. 2011, *ApJ*, 726, 82
- Cowan, N. B., & Agol, E. 2011b, *ApJ*, 729, 54
- Deleuil, M., Almenara, J.-M., Santerne, A., Barros, S. C. C., Havel, M., Hébrard, G., Bonomo, A. S., Bouchy, F., Bruno, G., Damiani, C., Díaz, R. F., Montagnier, G. & Moutou, C. 2014, *A&A*, 564, 56
- Deming, D., Seager, S., Richardson, L. J., & Harrington, J. 2005, *Nature*, 434, 740
- Demory, B.-O., Seager, S., Madhusudhan, N., Kjeldsen, H., Christensen-Dalsgaard, J., Gillon, M., Rowe, J. F., Welsh, W. F., Adams, E. R., Dupree, A., McCarthy, D., Kulesa, C., Borucki, W. J. & Koch, D. G. 2011, *ApJ*, 735, 12
- Demory, B.-O., de Wit, J., Lewis, N., Fortney, J., Zsom, A., Seager, S., Knutson, H., Heng, K., Madhusudhan, N., Gillon, M., Barclay, T., Desert, J.-M., Parmentier, V. & Cowan, N. B., 2013, *ApJ*, 776, 25
- Demory, B.-O. 2014, *ApJ*, 789, 20
- Désert, J.-M., Charbonneau, D., Fortney, J. J., Madhusudhan, N., Knutson, H. A., Fressin, F., Deming, D., Borucki, W. J., Brown, T. M., Caldwell, D., Ford, E. B., Gilliland, R. L., Latham, D. W., Marcy, G. W., Seager, S. 2011, *ApJS*, 197, 11
- Dickey, J. M., & Lientz, B.P. 1970, *The Annals of Mathematical Statistics*, 41, 214-226
- Esteves, L. J., De Mooij, E. J. W. & Jayawardhana, R. 2013, *ApJ*, 772, 51
- Foreman-Mackey, D., Hogg, D. W., Lang, D. & Goodman, J. 2013, *PASP*, 125, 306
- Fortney, J. J., Demory, B.-O., Désert, J.-M., Rowe, J., Marcy, G. W., Isaacson, H., Buchhave, L. A., Ciardi, D., Gautier, T. N., Batalha, N. M., Caldwell, D. A., Bryson, S. T., Nutzman, P., Jenkins, J. M., Howard, A., Charbonneau, D., Knutson, H. A., Howell, S. B., Everett, M., Fressin, F., Deming, D., Borucki, W. J., Brown, T. M., Ford, E. B., Gilliland, R. L., Latham, D. W., Miller, N., Seager, S., Fischer, D. A., Koch, D., Lissauer, J. J., Haas, M. R., Still, M., Lucas, P., Gillon, M., Christiansen, J. L. & Geary, J. C. 2011, *ApJS*, 197, 9
- Fulton, B. J., Petigura, E. A., Howard, A. W., Isaacson, H., Marcy, G. W., Cargile, P. A., Hebb, L., Weiss, L. M., Johnson, J. A., Morton, T. D., Sinukoff, E., Crossfield, I. J. M. & Hirsch, L. A. 2017, *AJ*, 154, 109
- Gandolfi, D., Parviainen, H., Deeg, H. J., Lanza, A. F., Fridlund, M., Prada Moroni, P. G., Alonso, R., Augusteijn, T., Cabrera, J., Evans, T., Geier, S., Hatzes, A. P., Holczer, T., Hoyer, S., Kangas, T., Mazeh, T., Pagano, I., Tal-Or, L. & Tingley, B. 2015, *A&A*, 576, 11
- Hansen, B. M. S. 2008, *ApJS*, 179, 484
- Heng, K. 2016, *ApJL*, 826, L16
- Hipke, M. & Angerhausen, D., 2015, *ApJ*, 811, 1
- Hu, R., Ehlmann, B. L., Seager, S., 2012, *ApJ*, 752, 7
- Hu, R., Demory, B.-O., Seager, S., Lewis, N., & Showman, A. P. 2015, *ApJ*, 802, 51
- Huber, P. J. 1981, *Robust Statistics*. New York: John Wiley and Sons
- Jenkins, J. M., Twicken, J. D., Batalha, N. M., et al. 2015, *AJ*, 150, 56
- Karkoschka, E. 1994, *Icarus*, 111, 174
- Kipping, D. M., Bakos, G. Á., Hartman, J., Torres, G., Shporer, A., Latham, D. W., Kovács, G., Noyes, R. W., Howard, A. W., Fischer, D. A., Johnson, J. A., Marcy, G. W., Béky, B., Perumilly, G., Esquerdo, G. A., Sasselov, D. D., Stefanik, R. P., Lázár, J., Papp, I. & Sári, P., 2010, *ApJ*, 725, 2017
- Kipping, D. M., Spiegel, D. S., 2011, *MNRAS*, 417, L88
- Kipping, D. M., Hartman, J., Buchhave, L. A., Schmitt, A. R., Bakos, G. Á. & Nesvorný, D. 2013, *ApJ*, 770, 101
- Knutson, H. A., Charbonneau, D., Allen, L. E., Fortney, J. J., Agol, E., Cowan, N. B., Showman, A. P., Cooper, C. S. & Megeath, S. T., 2007, *Nature*, 447, 183
- Lehmer, O. R. & Catling, D. C. 2017, *ApJ*, 845, 130
- Loeb, A. & Gaudi, S. B. 2003, *ApJ*, 588, 117
- Lopez, E. D. & Fortney, J. J. 2014, *ApJ*, 792, 1
- Lucy, L. B. & Sweeney, M. A. 1971, *AJ*, 76, 544
- Mallama, A. 2009, *Icarus*, 204, 11
- Mathur, S., Huber, D., Batalha, N. M., et al. 2017, *ApJS*, 229, 30

Mazeh, T. & Faigler, S. 2010, *A&A*, 521, 59

Mazeh, T., Nachmani, G., Holzer, T., Fabrycky, D. C., Ford, E. B., Sanchis-Ojeda, R., Sokol, G., Rowe, J. F., Zucker, S., Agol, E., Carter, J. A., Lissauer, J. J., Quintana, E. V., Ragozzine, D., Steffen, J. H. & Welsh, W., 2013, *ApJS*, 208, 16

Mcquillan, A., Mazeh, T. & Aigrain, S. 2014, *ApJS*, 211, 24

Morris, S. L. & Naftilan, S. A. 1993, *ApJ*, 419, 344

Rogers, L. A. 2015, *ApJ*, 801, 41

Rouan, D., Deeg, H. J., Demangeon, O., Samuel, B., Cavarroc, C., Fegley, B. & Léger, A. 2011, *ApJ*, 741, 30

Rowe, J., Borucki, W. J., Koch, D., Howell, S. B., Basri, G., Batalha, N., Brown, T. M., Caldwell, D., Cochran, W. D., Dunham, E., Dupree, A. K., Fortney, J. J., Gautier, T. N., Gilliland, R. L., Jenkins, J., Latham, D. W., Lissauer, J. J., Marcy, G., Monet, D. G., Sasselov, D., Welsh, W. F., 2010, *ApJ*, 713, 150

Rowe, J. & Thompson, S. E. 2015, arXiv e-prints: 1504.00707

Samsing, J. 2015, *ApJ*, 807, 65

Sanchis-Ojeda, R., Rappaport, S., Winn, J. N., Levine, A., Kotsen, M. C., Latham, D. W. & Buchhave, L. A. 2013, *ApJ*, 774, 54

Sandford, E. & Kipping, D. M., 2017, *AJ*, 154, 228

Santner, A., Bonomo, A. S., Hébrard, G., Deleuil, M., Moutou, C., Almenara, J.-M., Bouchy, F. & Díaz, R. F. 2011, *A&A*, 536, 70

Schwarz, G. E. 1978, *Annals of Statistics*, 6, 461

Seager, S. & Sasselov, D. D., 2000, *ApJ*, 537, 916

Seager, S., Whitney, B. A., & Sasselov, D. D. 2000, *ApJ*, 540, 504

Seager, S. & Mallén-Ornelas, G., 2003, *ApJ*, 585, 1038

Sheets, H. A. & Deming, D. 2014, *ApJ*, 794, 133

Sheets, H. A. & Deming, D. 2017, *AJ*, 154, 160

Shporer, A., O'Rourke, J. G., Knutson, H. A., Szabó, G. M., Zhao, M., Burrows, A., Fortney, J., Agol, E., Cowan, N. B., Desert, J.-M., Howard, A. W., Isaacson, H., Lewis, N. K., Showman, A. P. & Todorov, K. O. 2014, *ApJ*, 788, 92

Silverman, B. W., 1986, *Density Estimation for Statistics and Data Analysis*. London: Chapman and Hall

Sliski D. H., Kipping D. M., 2014, *ApJ*, 788, 148

Smith, J. C., Stumpe, M. C., Van Cleve, J. E., Jenkins, J. M., Barclay, T. S., Fanelli, M. N., Girouard, F. R., Kolodziejczak, J. J., McCauliff, S. D., Morris, R. L. & Twicken, J. D. 2012, *PASP*, 124, 1000

Snellen, I. A. G., de Kok, R. J., de Mooij, E. J. W. & Albrecht, S., 2010, *Nature*, 465, 1049

Spiegel, David S., Burrows, A., Ibgui, L., Hubeny, I., & Milsom, J. A. 2010, *ApJ*, 709, 149

Stumpe, M. C., Smith, J. C., Van Cleve, J. E., Twicken, J. D., Barclay, T. S., Fanelli, M. N., Girouard, F. R., Jenkins, J. M., Kolodziejczak, J. J., McCauliff, S. D. & Morris, R. L. 2012, *PASP*, 124, 985

Sudarsky, D., Burrows, A., Pinto, P. 2000, *ApJ*, 538, 885

Teachey, A., Kipping, D. M. & Schmitt, A. 2018, *AJ*, 155, 36

Thompson, S. E., 2015, *Kepler Data Release 24 Notes*, KSCI-19064-002, (Moffett Field: NASA Ames Research Center).

Winn, J. N., 2010, "Transits & Occultations" in "EXOPLANETS", eds. S. Seager, University of Arizona Press (Tucson, AZ)

Silverman, B. W., 1986, *Density Estimation for Statistics and Data Analysis*, Chapman & Hall, London.

**Table 4.** KOIs used in the Terran ensemble.

KOI	period [days]	planetary radius [ $R_{\oplus}$ ]
K02071.01	3.86	1.03
K04230.01	5.50	1.13
K01612.01	2.47	0.67
K01536.01	3.74	1.07
K05827.01	6.11	0.70
K02208.01	2.34	0.86
K02317.01	3.79	1.19
K01002.01	3.48	1.16
K04312.01	7.85	0.75
K04585.01	6.76	1.10
K02260.01	6.12	1.01
K02832.01	3.58	0.84
K04232.01	2.62	1.20
K02372.01	5.35	1.18
K04360.01	2.72	1.12
K03015.01	3.61	0.85
K02877.01	5.31	1.21
K01434.01	2.34	1.22
K03892.01	2.42	0.99
K02730.01	4.52	1.22
K04292.01	9.33	0.61
K03141.01	2.32	1.20
K04190.01	3.43	0.80
K02561.01	3.24	0.86
K02913.01	2.89	0.82
K02143.01	4.79	1.10
K02951.01	2.44	0.72
K04347.01	3.06	1.14
K01967.01	4.42	1.15
K04513.01	3.92	0.99
K02426.01	4.16	0.74
K02509.01	4.55	1.09
K04117.01	4.24	1.17
K01202.01	0.93	1.23
K04510.01	5.18	1.25
K03113.01	2.46	1.04
K02742.01	0.79	0.95
K02798.01	0.92	0.61
K01528.01	3.99	1.02
K02344.01	1.12	1.08
K02247.01	4.46	0.82
K02399.01	1.92	0.86
K02101.01	2.89	1.17
K02347.01	0.59	0.98
K01300.01	0.63	1.11
K02845.01	1.57	1.08
K02058.01	1.52	0.98
K02238.01	1.65	0.88
K04268.01	0.85	0.58
K02662.01	2.10	0.73

This paper has been typeset from a  $\text{\LaTeX}$  file prepared by the author.

**Table 5.** KOIs used in the Neptunian ensemble.

KOI	period [days]	planetary radius [ $R_{\oplus}$ ]	KOI	period [days]	planetary radius [ $R_{\oplus}$ ]
K00697.01	3.03	3.01	K02619.01	3.28	2.17
K00007.01	3.21	4.21	K01094.01	6.10	3.16
K01890.01	4.34	1.69	K01885.01	5.65	2.13
K00155.01	5.66	2.99	K02146.01	2.95	1.49
K01632.01	4.59	1.38	K02789.01	3.40	1.36
K00265.01	3.57	1.28	K00786.01	3.69	2.21
K01116.01	3.75	1.40	K01505.01	5.03	2.27
K01339.01	4.17	2.02	K02213.01	3.97	1.42
K01214.01	4.24	1.40	K02100.01	4.27	1.42
K01341.01	4.51	1.85	K04241.01	2.55	1.47
K01629.01	4.41	1.38	K01488.01	3.95	2.42
K00578.01	6.41	4.00	K02155.01	4.34	1.80
K02995.01	5.19	2.51	K02491.01	2.67	1.72
K02785.01	4.77	1.97	K01428.01	0.93	1.70
K00167.01	4.92	2.80	K00923.01	5.74	3.65
K02437.01	4.15	1.79	K01626.01	2.53	1.87
K02552.01	3.66	1.36	K02223.01	1.10	1.64
K00452.01	3.71	2.55	K02355.01	1.22	1.62
K02331.01	2.83	1.30	K01511.01	2.58	1.81
K02440.01	4.87	1.31	K02266.01	1.00	1.69
K00292.01	2.59	1.43	K03848.01	1.85	1.69
K03120.01	4.14	1.49	K00826.01	6.37	2.74
K00955.01	7.04	2.87	K00483.01	4.80	2.75
K02778.01	2.22	1.64	K01965.01	2.51	1.44
K02200.01	3.17	1.68	K00769.01	4.28	2.58
K01526.01	4.44	1.64	K00844.01	3.71	4.79
K00240.01	4.29	4.47	K00472.01	4.24	3.64
K03110.01	4.48	1.37	K02580.01	3.12	1.87
K00535.01	5.85	3.87	K01337.01	1.92	1.37
K04139.01	3.74	1.56	K01882.01	3.77	2.08
K00893.01	4.41	2.59	K00585.01	3.72	2.50
K01491.01	3.15	2.10	K01501.01	2.62	1.64
K02780.01	3.35	2.37	K01893.01	3.55	1.48
K01570.01	6.34	3.31	K00144.01	4.18	3.08
K02016.01	4.31	1.99	K04566.01	3.95	1.65
K00069.01	4.73	1.48	K02820.01	3.01	1.37
K00926.01	3.17	4.43	K01344.01	4.49	1.30
K00852.01	3.76	2.40	K00943.01	3.60	2.38
K01603.01	3.02	1.49	K02063.01	3.01	1.49
K01706.01	1.92	1.40	K00910.01	5.39	2.90
K00532.01	4.22	2.93	K01142.01	3.76	1.81
K00714.01	4.18	2.63	K00873.01	4.35	2.34
K02383.01	4.37	1.62	K02214.01	2.35	1.40
K01979.01	2.71	1.30	K01637.01	2.97	1.92
K01481.01	5.10	3.22	K00861.01	2.24	1.54
K00916.01	3.31	3.94	K02708.01	0.87	1.71
K02300.01	2.69	1.31	K01424.01	1.22	1.64
K00762.01	4.50	2.49	K01973.01	3.29	1.55
K01641.01	4.85	1.52	K00104.01	2.51	3.15
K00537.01	2.82	2.48	K02839.01	2.16	1.34
K00794.01	2.54	2.10	K01880.01	1.15	1.36
K00583.01	2.44	1.91	K01577.01	2.81	1.49
K00161.01	3.11	2.48	K00739.01	1.29	1.45
K01304.01	4.60	1.98	K02156.01	2.85	1.75
K02615.01	4.70	1.70	K00778.01	2.24	1.69
K05466.01	4.10	1.55	K02705.01	2.89	1.34
K00863.01	3.17	3.15	K04928.01	3.29	5.47
K00361.01	3.25	1.51			

continued to the right...